

Kolmogorov cascade as the governing mechanism for intervortex spacing in quantum turbulence

Clément Bret, Pantxo Diribarne,* Jérôme Duplat, and Bernard Rousset
dsBT/IRIG CEA, Université Grenoble Alpes - F-38054 Grenoble, France

(Dated: September 3, 2025)

In this paper, we investigate inertially forced isothermal quantum turbulence (the coflow of normal and superfluid components) at temperatures of 1.6 and 2 K. The experiments are carried out in a large optical cryostat, where quasi-isotropic, homogeneous turbulence is generated using a double oscillating grid. Turbulence intensity is tuned by varying the grid stroke and frequency. The flow is probed via two-dimensional (2D) and three-dimensional (3D) reconstructions of quasi-isodense microsphere trajectories, from which we extract the large-scale properties of the flow in the fully turbulent regime for different Reynolds numbers: the turbulent velocity fluctuations, the energy transfer rate, and the integral length scale. Additionally, we determine the mean vortex line density \mathcal{L} via attenuation of a second sound standing wave across the entire measurement volume. Our results confirm with an improved accuracy that the intervortex spacing $\ell = 1/\sqrt{\mathcal{L}}$ scales with the Reynolds number Re_κ (based on the quantum of circulation κ) as $\ell \propto \text{Re}_\kappa^{-3/4}$, with a well-defined numerical prefactor and no observed temperature dependence. This scaling recalls that of the dissipative length scale in classical Kolmogorov (K41) turbulence and it lead previous authors to interpret ℓ as an effective dissipation length scale. However, in our temperature range, this interpretation is not consistent with the apparent temperature independence of the prefactor. Based on those arguments, we propose an alternative interpretation that suggests that the inter-vortex distance in coflow turbulence is the consequence of the quantum restricted depth of the superfluid component energy cascade.

I. INERTIALLY FORCED QUANTUM VERSUS CLASSICAL TURBULENCE

Since the pioneering experiments of the 1920s [1, 2], ^4He has been known to exist in two distinct liquid phases below and above the so-called λ -transition ($T_\lambda = 2.1768$ K at atmospheric pressure), referred to as He I and He II by Keesom and Wolfke [3], due to their very different thermodynamic properties. In the 1930s, Kapitza [4] dubbed the He II phase a “superfluid” because of its ability to flow without viscosity through microscopic interstices, exhibiting behavior that is neither laminar nor turbulent, as observed by Allen and Misener [5] in thin capillaries. These peculiar observations combined with insights from the Bose-Einstein condensation theory motivated theorists such as London [6], Tisza [7], and Landau [8] to develop the so-called two-fluid model in the 1940s. This framework describes He II as a mixture of two interpenetrating components: a viscous normal component carrying all entropy and a superfluid component flowing without any viscosity. The proportion of each component evolves with temperature, with the superfluid fraction increasing as the temperature decreases toward 0 K. Further experimental evidence from Osborne [9] in the 1950s demonstrated that, despite being free of viscosity, the superfluid component can sustain circulation. This paradox was resolved by introducing quantum vortex lines, first proposed by Onsager [10] and later developed by Feynman [11]. These singular “topological defects” in the superfluid velocity field can be viewed as Ångström-scale vortex filaments with quantized circulation, $\kappa = h/m \approx 9.97 \times 10^{-8} \text{ m}^2/\text{s}$, where h is Planck’s constant and m is the atomic mass of ^4He . Under inertial forcing, where both components are synchronously driven at large scales by pressure gradients or mechanical stirring (e.g., in a von Kármán flow), He-II can enter a coflow Quantum Turbulent state. In this regime, vortex lines form a tangled structure that serves as the backbone of the superfluid velocity field, while the normal component organizes into classical multi-scale eddies in the manner of Richardson. Notably, these vortex lines also mediate the coupling between the normal and superfluid velocity fields: as they move

* pantxo.diribarne@univ-grenoble-alpes.fr

relative to the normal component, they experience a “mutual friction force” allowing for momentum exchange as originally described by Hall *et al.* [12, 13] and Bekarevich and Khalatnikov [14] in the 1950s. More recently, experiments were conducted to characterize the differences between classical and quantum turbulent flows. In the late 1990s, driven by applications in large-scale refrigeration (such as superconducting magnets for fusion or particle accelerators), measurements of pressure drop in He II at high Reynolds numbers (greater than 10^6) were conducted in pipes with centimeter-scale diameters and lengths spanning several meters (see, e.g., Refs. [15–17]). These studies revealed that, under these conditions, turbulent He II flow behaves similarly to classical fluids. The pressure drop through the pipe, $\Delta P \propto v^2$, holds for velocities v typically determined from the mass flow rate passing through the pipe and the associated friction coefficients resemble those found for classical flows. As mentioned previously, note that this is not the case for He II flow in thin capillary [5]. Global calorimetric measurements in the *Superfluid High REynolds von Kármán experiment* [18] further emphasized this similarity, demonstrating that the energy injected at large scales is identical in He I and He II [19]. Local velocity measurements using total head pressure tubes in various flow configurations also showed that the $E(k) \propto k^{-5/3}$ energy spectrum and the 4/5-th law can be applied in He II up to intermediate scales [20–22]. This confirms the existence of an inertial range and suggests a locking between the two velocity fields, \mathbf{v}_n and \mathbf{v}_s , within these scales. This locking argument is further supported by numerical simulations [23, 24] and theoretical considerations [25, 26]. The origin of this coupling is a direct consequence of the mutual friction force \mathbf{f}_{mf} , which tends to smooth out the velocity differences between the superfluid and normal components. However, the velocity fields \mathbf{v}_n and \mathbf{v}_s cannot be perfectly “locked” because, at scales smaller than the mean inter-vortex distance ℓ , where the superfluid velocity field is primarily governed by the nearest quantum vortex lines. Moreover, only the normal component experiences viscous dissipation. Thus, at some sufficiently small scale He I and He II turbulence should behave differently and mutual friction may be responsible for a part of the dissipation. The latter could be expected, at least within the temperature range from 2.15 K to 1 K, where both the normal and superfluid components constitute more than 1% of the total fluid density. Determining the decoupling scale and the effective dissipation mechanisms below it remains an open question. A promising approach to addressing this challenge likely lies in developing a deeper understanding of the so-called effective viscosity ν_{eff} of quantum turbulence. This concept was first introduced by Stalp *et al.* [27] in the 1990s to explain the observed classical-like scaling, $\mathcal{L} \propto t^{-3/2}$, in the decay of the mean vortex line density, \mathcal{L} , as a function of the time t after which a grid was towed in a finite channel. Associating $\langle (\kappa \mathcal{L})^2 \rangle$ to the variance of the coarse-grained vorticity field of the superfluid component $\langle \omega_s^2 \rangle \approx \langle \kappa \mathcal{L}^2 \rangle$, the authors drew an analogy to classical turbulence to express the energy dissipation rate ϵ as

$$\epsilon = \nu_{\text{eff}} \langle (\kappa \mathcal{L})^2 \rangle. \quad (1)$$

By further assuming that after a brief initial period, the integral length scale L of the flow saturates at the channel diameter D , so that the spatial energy distribution follows a classical Kolmogorov spectrum, $E(k) = C \epsilon^{2/3} k^{-5/3}$ where $C \approx 1.6$ is the Kolmogorov constant, up to the scale $k = 2\pi/L = 2\pi/D$, they finally derived the decay of the mean vortex line density,

$$\mathcal{L}(t) = \frac{(3C)^{3/2} D}{2\pi \kappa \sqrt{\nu_{\text{eff}}}} t^{-3/2}. \quad (2)$$

These considerations provide a straightforward framework that effectively matches the experimental observations. Several attempts have been made to measure ν_{eff} and its temperature dependence in the original towed-grid configuration [28, 29], in a similar configuration where the temporal decay was studied behind a fixed grid [30], or in a spin-down experiment at lower temperatures [31]. Although the reported values are in reasonable agreement giving credit to the approach proposed by Stalp *et al.* [27], Eq. (1) lacks a theoretical justification and it remains unclear which dissipation mechanisms are captured by ν_{eff} .

In a more recent study, Babuin *et al.* [32] inferred ν_{eff} directly from Eq. (1) in a steady-state regime. They measured the mean vortex line density \mathcal{L} in a channel behind a grid (with their sensor probing

a region between 16 and 31 mesh sizes downstream of the grid) or directly in the channel without the grid as a function of the mean velocity V imposed in the channel. As they did not directly measure the mean dissipation rate ϵ , they estimated its value indirectly using the classical relation $\epsilon = u_{\text{rms}}^3/L$. For the grid configuration, to extrapolate the turbulent velocity fluctuation from the mean velocity V , they assumed a turbulence intensity of $\tau = u_{\text{rms}}/V = 9\%$ and they inferred an integral scale of $L = M$, where M is the grid mesh size. For the no-grid configuration, they proposed $\tau = 5\%$ and $L = d/2$, where d is the diameter of the capillaries in the honeycomb-type flow conditioner placed at the channel inlet. Across all tested temperatures from 1.18 K to 2.16 K, they did observe the $\mathcal{L} \propto V^{3/2}$ scaling predicted by Eq. (1) and were able to extract a value for ν_{eff} . Note that an equivalent formulation of Eq. (1) was proposed by Salort *et al.* [24]:

$$\frac{\ell}{L} = \beta \text{Re}_\kappa^{-3/4}, \quad (3)$$

where $\text{Re}_\kappa = u_{\text{rms}}L/\kappa$ is the Reynolds number based on the quantum of circulation κ , and β is related to ν_{eff} by $\nu_{\text{eff}} = \beta^4\kappa$. The formulation of Eq. (3) clearly resembles the classical Kolmogorov relation for the dissipative scale $\eta \propto \text{Re}^{-3/4}$. Based on these similarities, it is tempting to associate ℓ to the dissipative scale of quantum turbulence and see ν_{eff} as the effective viscosity arising from mutual friction. Assuming that mutual friction is responsible for the entire dissipation (i.e. no dissipation is due to classical viscosity associated with normal component fraction), Babuin *et al.* [32] proposed the following relation,

$$\epsilon = \epsilon_{mf} = \frac{\langle \mathbf{f}_{mf} \cdot \mathbf{v}_{ns} \rangle}{\rho} = \frac{B}{2} \frac{\rho_s \rho_n}{\rho^2} (\kappa \mathcal{L}) \langle \mathbf{v}_{ns}^2 \rangle, \quad (4)$$

where B is the temperature-dependent mutual friction parameter, ρ_s and ρ_n are the superfluid and normal component densities, respectively, and $\rho = \rho_s + \rho_n$ is the total bulk density. Assuming that $\langle \mathbf{v}_{ns}^2 \rangle$ can be approximated by the classical relation $\langle \mathbf{v}_{ns}^2 \rangle = \gamma \kappa^2 / \ell^2$ (where γ is an adjustable dimensionless coefficient), an analytical expression for ν_{eff} (or equivalently β) follows:

$$\nu_{\text{eff}} = \gamma \frac{B}{2} \frac{\rho_s \rho_n}{\rho^2} \kappa. \quad (5)$$

As the measured values of ν_{eff} exhibited little to no dependence on temperature within the explored range (1.18 to 2.16 K), it appears that Eq. (5) does not accurately describe the data. Furthermore, the indirect estimation of ϵ introduced an uncertainty of about a factor of 10 in ν_{eff} , making any quantitative discussion relatively delicate.

From a broader perspective, an examination of the experimental dataset for ν_{eff} in the literature – derived from both decaying and steady-state turbulence experiments – reveals that, while the values remain within the same order of magnitude, the data appear relatively scattered (by a factor of ~ 3 to 4). A more accurate and well-characterized experimental determination of ν_{eff} , free from the ambiguities related to large-scale properties, would be a crucial milestone for both gaining a deeper understanding of the origin of Eq. (1) and testing the validity of Eq. (5). Additionally, such measurements could contribute to the validation of numerical models.

This paper presents what we believe to be the first direct experimental measurement of ν_{eff} in a stationary oscillating-grid turbulent flow at temperatures of 1.6 and 2 K. By “direct measurement,” we refer to the independent evaluation of large-scale flow properties, from which we extract both the mean energy dissipation rate ϵ and the mean vortex line density \mathcal{L} . We show that these measurements agree quantitatively with the traditional scalings of the K41 turbulent cascade. This provides insights into the energy cascade and dissipation mechanisms, leading us to propose a new paradigm and adaptation of Richardson’s cascade for He II turbulent flow.

II. EXPERIMENTAL SETUP

The measurements presented in this article were conducted within the Oscillating Grid Experiment in Superfluid (OGRES) experiment, which consists of a cylindrical cryostat with optical access windows. Compared to other experiments that study He II hydrodynamics through direct visualization [33–35], this setup is relatively large, with the generated flow involving approximately 5 L of liquid helium. The setup has been described in previous works [36–38], however, due to recent substantial modifications, this section presents the updated version along with the operational procedure developed to maintain stable thermodynamic conditions in both the He I and He II phases.

A. New OGRES setup

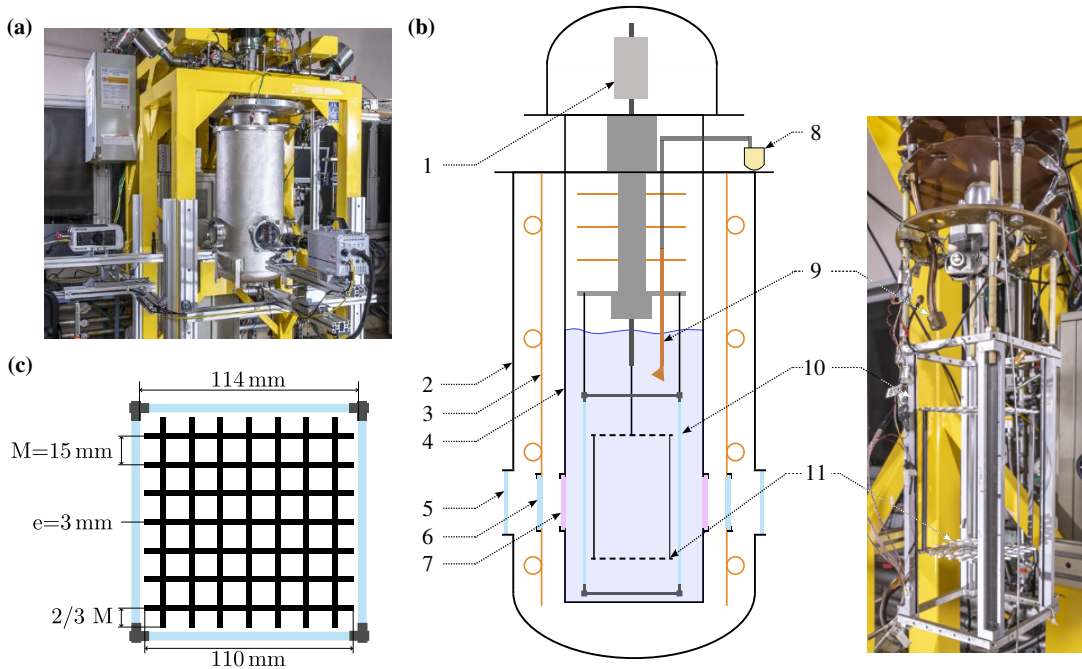


FIG. 1. (a) Global view of the updated OGRES experiment. (b) Detailed schematic: 1- linear motor, 2- outer stainless-steel vessel, 3- copper thermal shield with liquid nitrogen cooling coil, 4- inner stainless-steel vessel, 5- circular borosilicate window, 6- square borosilicate window, 7- square sapphire window, 8- seeding particle reservoir, 9- injector nozzle, 10- confinement tunnel, 11- double grid. (c) Detailed grid geometry.

As shown in Figs. 1(a) and 1(b), the cryostat consists of two nested stainless-steel vessels (item 2 and 4 in Fig. 1(b)) separated by an insulating vacuum gap. To reduce radiative heat transfer, a copper thermal shield (item 3) – wrapped in multi-layer insulation (MLI) and cooled to approximately 100 K using liquid nitrogen – is placed within the vacuum gap. Since the primary objective of the experiment is to directly visualize the flow inside the cryostat, each of the three concentric vessels is fitted with four windows (item 5, 6 and 7), each approximately 10 cm \times 10 cm in size, positioned at 90-degree intervals around the perimeter.

The inner vessel (item 4) has a diameter of 210 mm and can hold up to approximately 600 mm of liquid helium when filled to about two-thirds of its capacity. The temperature of the helium bath can then be adjusted by controlling the pressure inside the vessel, allowing for measurements both above and below the λ -transition.

The flow under investigation is generated in a 300 mm high confinement tunnel (item 10) with a square cross-section of 114 mm \times 114 mm, using an oscillating double-grid (item 11). The grid geometry, illustrated in Fig. 1(b), is the same as the one utilized in the previous studies [37, 38]. The mesh size is $M = 15$ mm, and the grids consist of a 6×6 matrix of meshes, with an additional $2/3$ mesh at the edges. The bars have a square cross-section of 3 mm thickness, resulting in a solid fraction of 34.5%. The two grids are separated by a distance $H = 167$ mm. This configuration, as reported in the literature [39, 40], is known to enhance the homogeneity of turbulence properties in the direction perpendicular to the grids. For sufficiently large grid spacing (i.e. $H/M > 5$), Shy *et al.* [40] observed that the turbulent velocity fluctuations became homogeneous over a band approximately $H/2$ wide, centered on the midplane.

The grids are oscillated using a linear motor, which allows for continuous adjustment of the stroke ($S_{\text{mot}} \in [0, 32]$ mm) and frequency ($f_{\text{mot}} \in [0, 12]$ Hz), leading to a wide range of forcing intensities within a single experimental campaign (u_{rms} up to 30 mm/s).

B. Operating procedure

In the He I phase, temperature gradients driven by heat inputs (of order 2 W) can easily exceed the spinodal temperature due to the poor thermal conductivity of He I, leading to nucleate boiling at the inner vessel walls. To perform undisturbed measurements, it is thus essential to subcool the liquid in the confinement tunnel to prevent boiling. To ensure the reproducibility of our measurements, a systematic procedure was developed: first, the vessel pressure is reduced to 52 mbar, cooling the bath to a uniform $T \approx 2.2$ K. Once this temperature is reached, the pressure is rapidly increased to 100 mbar, effectively stopping the boiling in the core of the bath. This allows for several minutes of turbulence measurements, during which the temperature drift remains lower than 0.3 K, ensuring that relative variations in density and dynamic viscosity are kept under 1%. Once the measurements are completed, the pumping cycle is repeated. During each recoiling phase, the liquid level gradually drops. The cryostat is refilled as soon as the liquid height approaches the top of the confinement tunnel.

In the He II phase, as observed nearly a century ago [41], the bath does not boil below the λ -transition because of the very high apparent thermal conductivity of superfluid helium. Consequently, turbulence measurements can be performed directly at saturation temperature. The pressure is adjusted to achieve the desired temperature (1.6 K or 2 K in the reported measurements), and the bath pressure regulation system is activated to ensure temperature stability, which is essential for the readability of second sound measurements (see Sec. III B 3 for a detailed discussion).

III. MEASUREMENT SYSTEMS

We adopt two independent and complementary approaches to obtain a complete description of the properties of the flow. The first approach involves visualization systems that capture trajectories of particles seeded in the flow. Two distinct systems are employed: one reconstructs 3D trajectories, while the other only reconstructs $2 \times 2D$ trajectories. The second approach, applied exclusively in He II, analyzes the attenuation of a stationary second sound wave as it interacts with quantum vortex lines present in the flow. In this section, we present the characterization of the particle properties (size and density), followed by an overview of the two visualization systems, and finally, a description of the second sound resonant cavity, from its fundamental principles to its effective operating procedure.

A. Particle tracking velocimetry

1. Particle characteristics and injection system

To seed the flow with small, monodisperse tracers, a new technique is currently being developed in the laboratory to generate solid spherical deuterium particles, a few microns in diameter, by dropping liquid droplets above the bath [42]. For this study, however, we opted for a simpler alternative: microspheres with a hollow core and a glass shell. The ones we use, supplied by Microsphere Technology Ltd., have a specified density of 140 kg/m^3 and diameters ranging from 75 to $90 \mu\text{m}$. To eliminate any potential uncertainties, we conducted direct measurements to verify these values.

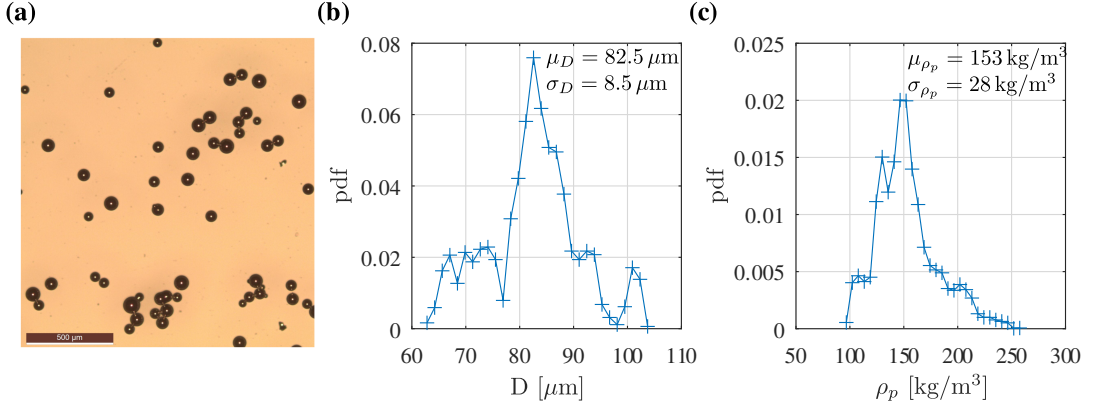


FIG. 2. (a) Optical microscope image (top view). Illumination from above creates a small white dot on the top of each particle due to light reflection. (b) Distribution of particle diameters. (c) Distribution of particle densities, deduced from Eq. (6).

To assess the properties of the particles, we first examined their shape under an optical microscope to qualitatively confirm their sphericity [see Fig. 2(a)]. To further validate their reported properties, we measured both the diameter and the terminal velocity of a few thousand particles falling freely in an air cavity. The diameter distribution is shown in Fig. 2(b) and matches relatively well with the range announced by the manufacturer (we found a mean diameter $\mu_D = 82.5 \mu\text{m}$ and a standard deviation $\sigma_D = 8.5 \mu\text{m}$). According to Stokes' law – assuming that the flow around the falling particles is laminar – the sedimentation velocity v_{sed} for a particle of density ρ_p falling through a fluid at rest of density ρ_f and dynamic viscosity μ_f is given by:

$$v_{\text{sed}} = \frac{1}{18} \frac{(\rho_p - \rho_f) D^2 g}{\mu_f}, \quad (6)$$

where g is the gravity acceleration. This relationship allowed us to deduce the particles densities from their terminal velocity and diameter. The results are reported in Fig. 2(c) and yield a particle density distribution with a mean of $\mu_{\rho_p} = 153 \text{ kg/m}^3$ and a relatively large standard deviation of $\sigma_{\rho_p} = 28 \text{ kg/m}^3$.

To seed the particles into the cryogenic helium flow, we designed a specialized setup (see Fig. 1(b)). It consists of an independent circuit with a 20 cL particle reservoir, which is connected to a conical nozzle located directly above the confinement tunnel. The reservoir can be isolated from the cryostat to be filled with particles and then connected alternatively to a vacuum pump and a pressurized helium gas bottle to rinse the particles, ensuring a clean mixture of helium gas and particles without air. Once prepared, the mixture is pressurized to 300 mbar above the bath pressure and injected into the flow by opening an electromechanical valve. This setup addresses the clogging issues that limited previous

injection methods used in Ref. [37]. Furthermore, it allows the particle reservoir to be refilled without interrupting the experiment and improves reproducibility by enabling synchronized data acquisition (e.g., imaging and second sound measurements) with particle injection.

In practice, after the injection of the particles, we typically wait for about 30 s to let sedimentation remove the heaviest and lightest particles from the measurement volume. However, despite those precautions, we observe that the residual characteristic sedimentation velocity is non-negligible (of the order of a few millimeters per second), and may vary slightly between runs (for more details refer to Ref. [43]). Therefore, special care must be taken when analyzing particle motion and velocity along the vertical axis as gravity introduces a bias.

2. 3D visualization system

The system used to capture and reconstruct the three-dimensional trajectories of particles in the flow is the LaVision “MiniShaker.” It consists of a box of four pre-aligned cameras and a high-power LED panel to illuminate the particles within the flow [see Fig. 3(a)]. The measurement volume is approximately $80 \times 80 \times 80 \text{ mm}^3$.

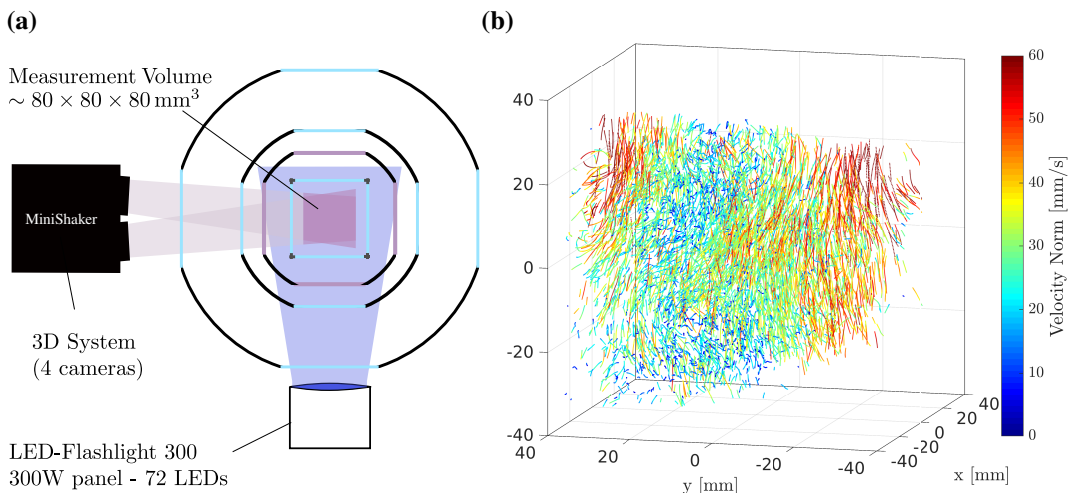


FIG. 3. (a) Top view of the 3D setup. An estimate of the measurement volume at the center of the confinement tunnel is represented by the intersection of the two visualization beams of the cameras. (b) Example of reconstructed 3D turbulent trajectories (He II at 2 K). The norm of the velocity, represented in color, is calculated by convolution with a Gaussian derivative kernel with a characteristic time of four time steps ($\sim 18 \text{ ms}$).

Each camera has a resolution of $1216 \times 1000 \text{ px}^2$ sensor, leading to a spatial resolution of $64.4 \mu\text{m}/\text{px}$. The frame rate is set to 220 Hz and the exposure time is adjusted to $200 \mu\text{s}$ to avoid motion blur for particles moving at velocities of up to 100 mm/s (displacement $< 0.3 \text{ px}$ during the exposure time). The system can store up to 29000 images per run, providing over two minutes of data acquisition, which is enough to capture the relevant large scale flow dynamics, considering the flow’s characteristic time scale is of the order of one second.

Calibration is performed using a 3D target placed in the measurement volume. Each of the four cameras captured images of the calibration plate, allowing the LaVision software to initialize the optical transfer function (OTF) and define a unified coordinate system. Due to spatial constraints, calibration is conducted only at room temperature. To account for the minor refractive index differences between air and liquid helium, we take advantage of the auto-calibration step which iteratively refines the OTF

by detecting the 3D particle positions directly from flow images and back-projecting the centroid positions onto the two-dimensional (2D) images, reducing error to a standard deviation of 0.2 to 0.3 px.

Particle trajectories are then reconstructed using the “Shake The Box” method, which allows us to obtain trajectories for four runs in He II at 2 K. These trajectories span from 20 time steps to over 2000, with an average of 50 time steps per trajectory, capturing around 7000 particles within the 3D measurement volume at each time step [see Fig. 3(b)].

3. 2×2D visualization system

The second system captures 2×2D particle trajectories at higher temporal and spatial resolution using two synchronized high-speed cameras positioned orthogonally (see Fig. 4(a)).

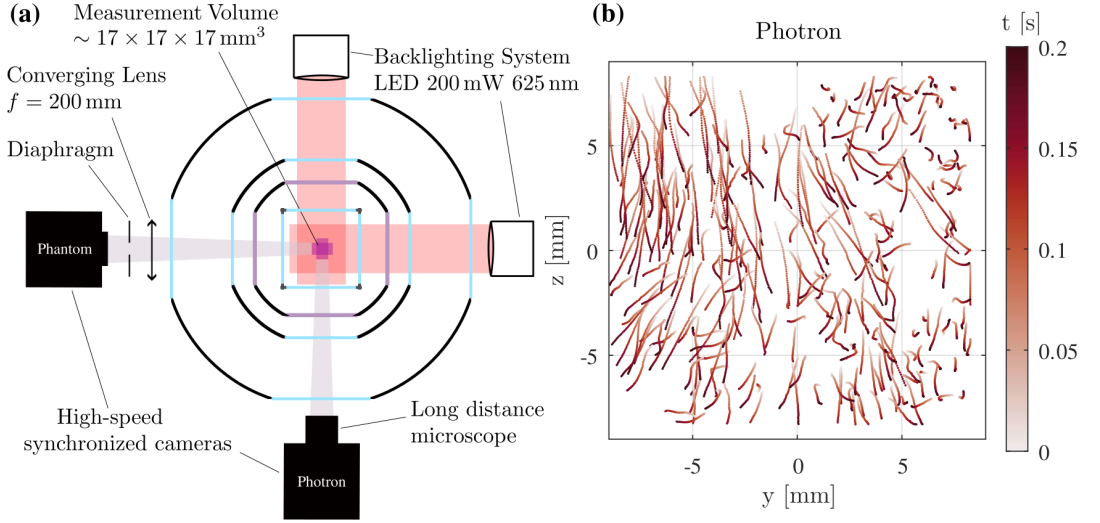


FIG. 4. (a) Top view of the 2×2D setup. An estimate of the measurement volume at the center of the confinement tunnel is represented by the intersection of the two visualization beams of the cameras. (b) Example of reconstructed 2D turbulent trajectories.

The Phantom V311 is operated without a standard camera lens. Instead, a plano-convex converging lens with a focal length of 200 mm is placed at an appropriate distance to achieve the desired magnification. The Photron Fastcam SA5, on the other hand, is equipped with a long-distance microscope (Infinity Model K2/SC). Note that a key constraint is ensuring that the optics’ working distance is sufficient to keep them outside the cryostat. Both cameras are set to an 800×800 px² resolution, yielding a field of view of approximately 17×17 mm². Compared to the previous system, lighting is provided by directly illuminating the camera with 625 nm-red LEDs (M625L4-C4) in a back-light configuration. In this setup, particles within the depth of field shadow the light, appearing as sharp black circles on a white background. Note that the LED power required is significantly lower than that of the 3D system (~ 1000 times less for a shutter ten times shorter).

This configuration introduces the challenge of determining whether a particle lies within the depth of field. As a particle moves out of the core of the depth of field, it gradually shifts from a sharp black disk to a larger blurred gray disk before fully disappearing. This gradual defocusing introduces ambiguity. To address this, we developed an objective method based on Helmlí and Scherer [44]’s “Mean Method” to measure the camera’s effective depth of field (for more details French-speaking readers can refer to Ref. [43]). The diaphragm aperture is adjusted to achieve a depth of field of approximately 30 mm.

At room temperature, to center the fields of view of the two cameras and measured the scale factors,

we suspended a 6 mm calibrated sphere inside the cryostat using the sealing port for the helium transfer. The sphere is placed at the center of the confinement tunnel and the cameras and lights are adjusted to focus on it. After fully opening the apertures to minimize depth of field, the calibration images are captured. The apertures are then closed back to obtain appropriate depths of field and the sphere is removed. The resulting scale factors are approximately $20.4 \mu\text{m}/\text{px}$ for the Phantom V311 and $20.7 \mu\text{m}/\text{px}$ for the Photron Fastcam SA5.

During turbulence measurement, images are captured at a high frame rate of 3000 Hz. To prevent the cameras memory from saturating in just 4 seconds, the data acquisition is divided into 19 segments of 600 images, each separated by approximately 2 s, with the aim of capturing distinct realizations of the flow. The exposure time is set to $20 \mu\text{s}$ to avoid motion blur for particles moving at velocities of up to 100 mm/s (displacement $< 0.1 \text{ px}$ during the exposure time).

To reconstruct the trajectories from the images, we employ a classic particle tracking algorithm, which typically consists of a detection phase followed by a predictive association phase. We obtain 36 runs in He I, He II (2 K), and He II (1.6 K). Figure 4(b) shows a selection of long trajectories reconstructed from a segment of a He I run.

B. Second sound resonant cavity

1. Principle

Deriving the propagation of an isobaric and isochoric temperature perturbation through an isotropic vortex tangle with a mean vortex line density \mathcal{L} in the so-called acoustic approximation, we obtain the following equation (see appendix of Ref. [45] for a step by step derivation):

$$\frac{\partial^2 T}{\partial t^2} = c_2^2 \nabla^2 T - 2\alpha_{\mathcal{L}} c_2 \frac{\partial T}{\partial t} \quad (7)$$

where

$$c_2 = \sqrt{\frac{\rho_{s,0}}{\rho_{n,0}} \frac{\sigma_0}{C_p}} \sqrt{\sigma_0 T_0} \quad \text{and} \quad \alpha_{\mathcal{L}} = \frac{B\kappa}{6c_2} \mathcal{L}. \quad (8)$$

Equation (7) can be read as a d'Alembert equation with a damping term $\alpha_{\mathcal{L}}$, indicating that the temperature perturbation propagates as a wave with velocity $c_2 \sim 15\text{-}20 \text{ m/s}$, the so-called “second sound velocity,” by analogy to the propagation velocity of isothermal and isentropic pressure perturbation (i.e. ordinary sound wave). Moreover, as shown by Eq. (8), the temperature perturbation is damped by the presence of vortex lines. By measuring this attenuation, one can deduce the vortex line density.

In practice, we set up a second sound standing wave across the confinement tunnel at the grids midplane. The physics of such a resonant cavity can be described by the following expression, which gives the complex amplitude of the standing wave measured by the receptor (see, e.g., Refs. [46, 47] for further details),

$$\tilde{U} = \frac{U_0 e^{-i(\phi_{cl} + \phi_{el})}}{\cosh(i\pi \frac{2L}{c_2} f - i\phi_{cl} + \alpha L)} \quad (9)$$

where U_0 is the amplitude of the wave generated by the emitter, ϕ_{cl} the phase shift determined by the boundary conditions and ϕ_{el} the phase shift introduced by the measurement chain. The damping coefficient $\alpha = \alpha_0 + \alpha_{\mathcal{L}}$ account for both α_0 , the intrinsic damping of the cavity mostly due to geometrical effects, and $\alpha_{\mathcal{L}}$ the vortex tangle attenuation introduced previously.

If the excitation frequency f is chosen such that the wavelength $\lambda = c_2/f$ is a sub-multiple of the cavity length, the wave will resonate, accumulating energy and reaching a maximum amplitude given

by

$$U_{res} = \frac{U_0}{\sinh(\alpha L)}. \quad (10)$$

Given the high sensitivity of the resonant amplitude to the damping coefficient α , the simplest approach to assess the additional attenuation caused by quantum vortex lines when the motor is shaking is thus to set the excitation frequency at resonance and track the decrease in amplitude, $U(t)$. This signal can then be demodulated using Eqs. (10) and (8) as

$$\mathcal{L}(t) = \frac{6c_2}{B\kappa} \left[\frac{1}{L} \sinh^{-1} \left(\frac{U_0}{U(t)} \right) - \alpha_0 \right], \quad (11)$$

where α_0 and U_0 are calibrated by recording the maximum amplitude with the motor at rest. Note that, depending on the boundary conditions, the resonant wavelength is given by $\lambda_{res} = \frac{2L}{n - \frac{1}{2} + \frac{\phi_{cl}}{\pi}}$, where

$\phi_{cl} \in \left[-\frac{\pi}{2}, \frac{\pi}{2}\right]$ but the maximum amplitude given by Eq. (10) remains independent of ϕ_{cl} .

Equation (11), or a simpler first-order Taylor expansion version assuming $\alpha L \ll 1$, leading to

$$\mathcal{L}(t) = \frac{6c_2}{B\kappa} \alpha_0 \left(\frac{U_{res}}{U(t)} - 1 \right), \quad (12)$$

has been widely used in the literature to extract mean vortex line density from second sound attenuation (see, e.g., Varga *et al.* [46] for a historic review of “the use of second sound in experimental investigations of quantized vorticity and quantum turbulence”). However, as detailed in the Sec. III B 2, the operating range of our cavity around the 100th harmonic make it highly sensitive to parasitic temperature drifts and this simple procedure cannot be applied directly. More precisely, when the motor oscillates, the temperature fluctuations may be large enough to affect the value of the second sound velocity c_2 . This, in turn, changes the wavelength λ , shifting the cavity out of resonance and “artificially” reducing the measured amplitude (i.e., not because of the presence of vortex lines). One way to handle this effect is to record both the magnitude $U(t)$ and the phase $\theta(t)$ measured by the receptor and demodulate the complex amplitude $\tilde{U}(t) = U e^{i\theta(t)}$ as suggested by Eq. (9):

$$\begin{cases} \alpha(t) = \Re \left[\cosh^{-1} \left(\frac{U_0 e^{-i\phi_{cl}} e^{-i\phi_{el}}}{\tilde{U}(t)} \right) \right] / L \\ c_2(t) = 2\pi L f / \left\{ \Im \left[\cosh^{-1} \left(\frac{U_0 e^{-i\phi_{cl}} e^{-i\phi_{el}}}{\tilde{U}(t)} \right) \right] + \phi_{cl} + n\pi \right\}. \end{cases} \quad (13)$$

The mean vortex line signal $\mathcal{L}(t)$ can then straightforwardly be reconstructed as follows,

$$\mathcal{L}(t) = \frac{6c_2(t)}{B\kappa} (\alpha(t) - \alpha_0). \quad (14)$$

To apply this more refined approach, the parameters U_0 and α_0 must be calibrated first, as well as ϕ_{cl} and ϕ_{el} . This is done by fitting a frequency sweep of the resonance peak at a stable reference temperature with the motor at rest using Eq. (9). An example of this procedure in our setup at $T = 2$ K is illustrated in Fig. 5.

2. Set up

Both to excite the second sound wave within the resonant cavity and measure its amplitude and phase, we used oscillating superleak transducers (OST). Those transducers make use of a porous membrane that allows the superfluid component to pass through while being nearly impermeable to the

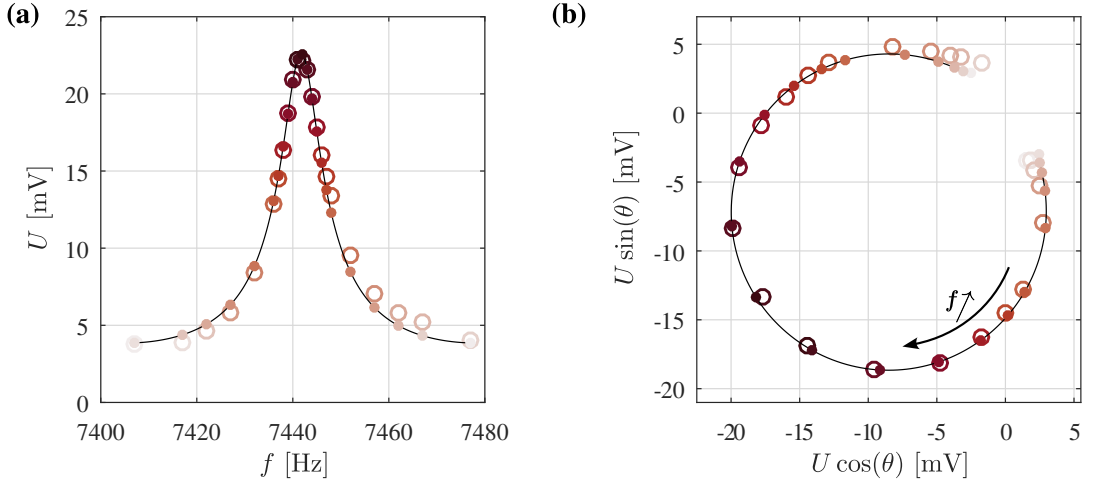


FIG. 5. Frequency sweep of the cavity without flow forcing (motor at rest). Open markers correspond to the measured values. Solid lines represent Eq. (9) after fitting the parameters $U_0 = 3.9$ mV, $\alpha_0 = 1.48$ m⁻¹, $\phi_{el} = 134^\circ$, $\phi_{cl} = 96^\circ$. Filled markers indicate the interpolated values at the same frequencies tested during the frequency sweeps (allowing phase tracking in the phase-amplitude representations). (a) Amplitude representation. (b) Polar representation.

normal fluid at times scales of the order of 1 ms and below. This selective permeability enables the membrane to either induce or detect oscillations in the local density ratio between the normal and superfluid components, which are an image of temperature oscillations. To ensure the measurement is as non-intrusive as possible, each transducer is integrated into a brass plate that can replace the glass panels of the confinement tunnel walls (see Fig. 1).

As illustrated in Fig. 6(a), the OSTs are designed following the Sell principle (see Ref. [48] for a detailed review). These capacitive electrostatic transducers are made of a fixed cathode (a copper plate located on the rear side) and a mobile anode (the membrane on the front side, in contact with the fluid).

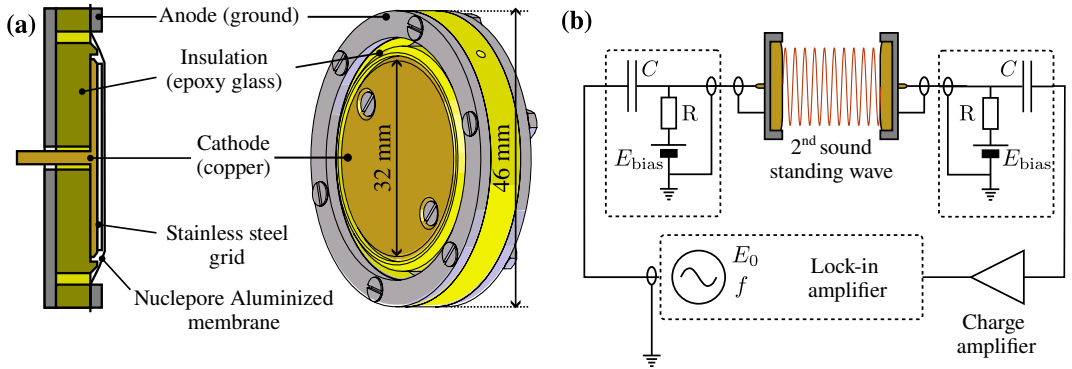


FIG. 6. Summary of the functioning of the resonant cavity components. (a) Detailed structure of the OSTs. (b) Control electronics, including the “bias box” composed of ten 9 V batteries and a high-pass filter ($R = 10$ M Ω and $C = 1$ μ F).

The porous membranes used are Whatman Nuclepore[®] 111705 membranes with characteristic pore diameters of 0.1 μ m. The front side of each membrane is coated with a 30 nm thick layer of aluminum deposited using a vacuum evaporation system. This method ensures directional deposition, leaving the pores, with diameters significantly larger than 30 nm, open. The membranes can then be used

as the anode of a capacitor, connected to the sensor chassis which are grounded. The rear face of the membranes is separated from the cathode by a stainless steel mesh with a $100\text{ }\mu\text{m}$ pitch and bar diameters of $30\text{ }\mu\text{m}$. The dielectric gap between the electrodes is structured to segment the sensor surface into multiple cavities, improving the flatness of the emitted wavefront [49] and enhancing the directionality of the receptor. This geometry is chosen to replicate the most efficient configuration reported in the study by Zimmermann [50]. The active area of the membrane has a diameter of 32 mm .

The membranes are bent over the grid cavities by applying a bias voltage of approximately $E_{\text{bias}} \approx 90\text{ V}$, generated by ten 9 V batteries connected in series. At the emitter, as summarized on Fig. 6(b), the membrane oscillation is driven by a sinusoidal voltage delivered by the output source of a lock-in amplifier (Stanford Research SR830) with adjustable frequency f and amplitude E_0 (up to 15 V by adding an amplifier) through an RC filter, thereby decoupling the source from the high voltage E_{bias} . As it emits a multitude of second sound waves originating from each cavity of the mesh, these numerous quasi-point waves interfere in such a way that, to a first approximation, their superposition can be considered equivalent to a single progressive plane wave. At the receiver, the second sound wave interacts with the membrane, generating a sinusoidal voltage response proportional to the amplitude of the oscillations. More precisely, the interaction causes variations in the apparent capacitance of the system, as the distance between the anode and cathode fluctuates. These capacitance variations produce charge oscillations, which are converted into voltage fluctuations by a charge amplifier (Stanford Research SR570). The amplifier is configured with a gain of $1\text{ V}/\mu\text{A}$ and a 12 dB/decade high-pass filter to reject low-frequency noise, with a cutoff frequency of 300 Hz , as the cavity operates at frequencies above 1 kHz (see Sec. III B 3). The output signal is then demodulated at frequency f by the lock-in amplifier to retrieve the amplitude $U(t)$ and phase $\theta(t)$. The time constant is set to 3 ms , which appears sufficient to reject most of the noise.

3. Operation procedure of the second sound resonant cavity

This section provides an overview of how we practically operate the cavity, based on the procedure presented in Sec. III B 1 and illustrated for a bath temperature of 2 K .

The first step is to select an operating harmonic by sweeping the excitation frequency and analyzing the amplitude response measured by the receptor. Figure 7(a) illustrates a frequency sweep performed with the cavity at rest, revealing successive second-sound resonant peaks around the 100th harmonic spaced by $\Delta f = c_2/2L \approx 75\text{ Hz}$ at 2 K . By exploring a wide range of excitation frequencies from 2 kHz to 40 kHz , we observe that the sensitivity of the system is optimal in this range. From this large frequency sweep, we also extract a precise value of the cavity length L using the following procedure: we identify $n_p = 517$ resonant peaks, with the first and last occurring at 2075 Hz and 39925 Hz , respectively. As the difference between these two values is given by $(n_p - 1)c_2/2L$, we obtain $L = 116\text{ mm}$, using the saturated value of $c_2 = 17\text{ m/s}$ corresponding to the measured cavity temperature from a Cernox[®] sensor, $T = 1.982 \pm 60 \times 10^{-6}\text{ K}$. The discrepancy between this cavity length and the tunnel width (114 mm) is likely due to the slight retraction of the OST front faces relative to the brass plates in which they are embedded.

Note that simple considerations of 2D effects can explain why the cavity cannot reliably be operated at lower harmonics: as the emitter diameter, $D = 32\text{ mm}$, introduces diffraction effects when the wavelength λ is of the same order of magnitude, we can estimate that to ensure more than 50% of the emitted beam interacts with the receptor, the system must operate above the 95th harmonic. Nevertheless, it is important to note that operating at such high harmonics makes the system highly sensitive to temperature fluctuations in the bath. The resonant frequency associated with the 100th harmonic is given by $f_{100} = c_2/\lambda_{100} = 100c_2/2L$, implying that fluctuations in c_2 due to temperature variations are amplified by a factor of 100 compared to the first harmonic. At 2 K , temperature changes as small as 0.1 mK – corresponding to pressure fluctuations of the order of $8\text{ }\mu\text{bar}$ – can shift the resonant frequency of the 100th harmonic by approximately 1 Hz . This shift causes the cavity to deviate slightly from resonance, as it will no longer be excited exactly at its resonant frequency. As highlighted in Sec. III B 1, it is therefore crucial to record the full complex amplitude $\tilde{U}(t) = U(t)e^{i\theta(t)}$

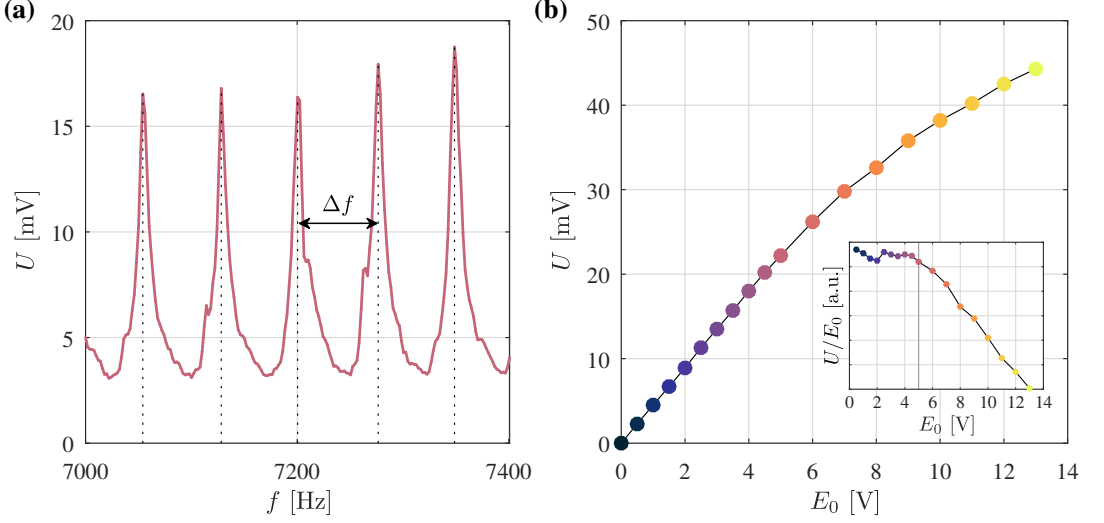


FIG. 7. (a) Amplitude U of the wave measured by the receiver as the excitation frequency of the emitter is swept (resolution of 2 Hz). Successive resonance peaks are observed approximately every 75 Hz, consistent with the expected behavior for a cavity of length $L = 116$ mm in a saturated bath at 30 mbar. The excitation input amplitude of the emitter is set to $E_0 = 5$ V (b) Amplitude U of the wave measured by the receiver at 2 K as a function of the excitation input amplitude E_0 of the emitter.

of the wave during turbulence measurements to disentangle amplitude attenuation caused by vortex lines from fluctuations due to temperature-induced resonance shifts.

Once the excitation frequency of the cavity is set, to maximize the signal to noise ratio, one has to choose the largest possible input amplitude E_0 while ensuring that the traveling counterflow wave does not itself produce parasitic quantum vortex lines (the so-called T1 transition). As shown in Fig. 7(b), the characteristic curve $U(E_0)$ remains within the linear response regime up to $E_0 = 5$ V which is the value used for all the measurements. Note that due to the unclear boundary conditions imposed at both ends of the cavity by the OSTs, it is not straightforward to estimate the associated counterflow velocity v_{ns} . A supplementary analysis using an alternate emitter (a heating plate) verified that the associated critical heat flux is about $\varphi_0 \approx 2$ W/m² leading to $v_{ns} = \varphi_0 / \rho_s \sigma T \approx 16$ μ m/s. The hydraulic diameter associated with the heating plate is $D_h = 4S/P \approx 50$ mm, where $P = 214$ mm is the perimeter of the heating and $S = 42 \times 65$ mm² is its surface. We thus deduce the critical Reynolds number, $Re_c = v_{ns} D_h / \kappa \approx 8.5$ in excellent agreement with the values compiled in Bertolaccini *et al.* [51]. As the product $\rho_s \sigma T$ monotonically increases when the temperature is lowered, the 5 V voltage value extracted at 2 K from Fig. 7(b) is a lower bound of the critical tension for temperature lower than 2 K. As every measurement report in this paper are made at $T \leq 2$ K, we can safely assume that the second sound standing wave never added parasitic vortex lines in the flow.

The following step is to measure the values of U_0 , α_0 , ϕ_{cl} and ϕ_{el} to set the reference point at resonance from which we will follow the evolution in the phase/amplitude plane to assess both the mean vortex line density of the flow and the temperature fluctuations. As shown in Fig. 5, this is done by sweeping the resonant peak associated with the selected harmonic while the motor is at rest and fitting the peak using Eq. (9). The second sound velocity, c_2 , is assumed to correspond to its saturation value under the given regulated pressure bath (30 mbar for Fig. 5) and the cavity length is fixed, $L = 116$ mm as previously discussed. Note that, as their values are imposed for the fit, the uncertainties on c_2 and L are encapsulated in the returned θ_{cl} value that loses its original meaning $\theta_{cl} \in [-\pi/2, \pi/2]$.

We finally choose the excitation frequency of the cavity to resonance and start the measurement. In the example of Fig. 5(a), the resonant frequency determined from the fit is 7441.7 Hz, and the

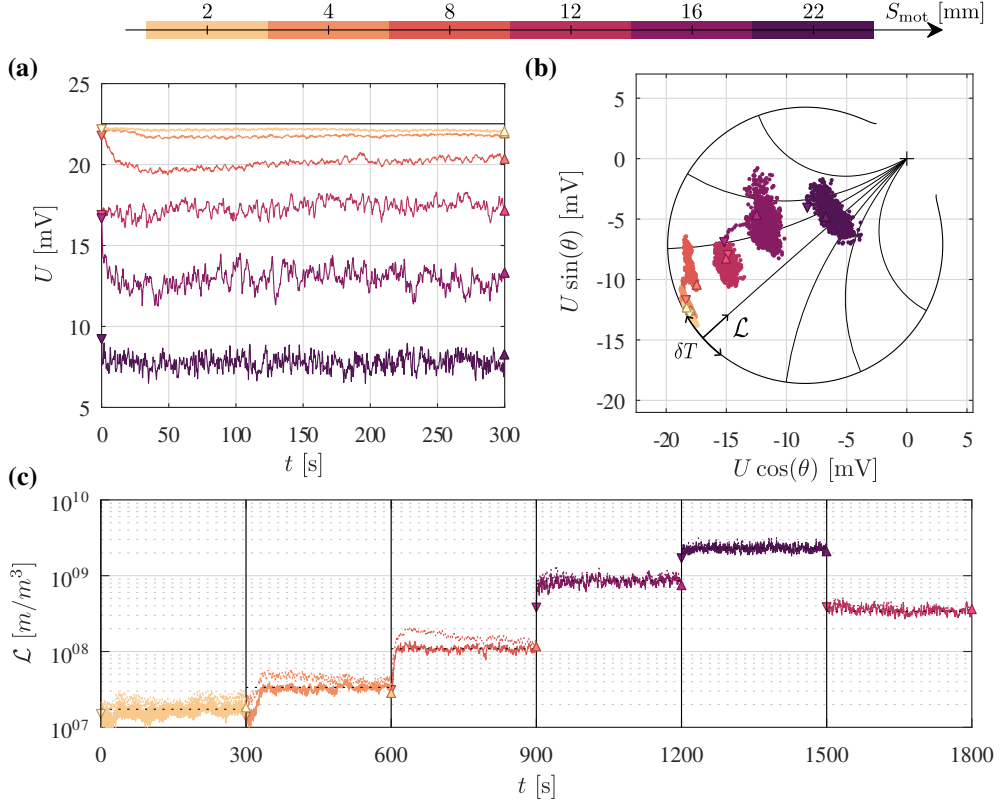


FIG. 8. Raw signals (at 2 K) measured at the output of the synchronous detection for a series of flow forcing at a grid oscillation frequency of $f_{\text{mot}} = 9$ Hz for different stroke amplitudes S_{mot} . The excitation frequency is set to $f_{\text{exc}} = 7442$ Hz (a) Amplitude, $U(t)$. The solid black line represents the maximum amplitude at resonance without vortex lines [see Eq. (10)], as deduced from the fit of Eq. (9) (see Fig. 5). (b) Signal trajectories in the polar plane. The pseudo-circle represents the complex amplitude of the 102nd harmonic of the cavity without vortex lines see Eq. (9). as deduced from the fit of Eq. (9) (see Fig. 5). The black rays show the trajectories of points kept at constant excitation frequency, while the attenuation coefficient is increased, providing a reference. (c) Mean vortex line density, \mathcal{L} . Solid lines show values obtained by demodulating both the phase $\theta(t)$ and amplitude $U(t)$ using Eqs. (13) and (14), while dotted lines show values obtained by demodulating only the amplitude $U(t)$ using Eq. (11).

excitation is set to the nearest integer, $f = 7442$ Hz, as the lock-in allow only integer frequencies. The proper turbulence measurements can then begin by recording the output signal [$X = U \cos(\theta)$ and $Y = U \sin(\theta)$ components from the lock-in detection] for 300 s for different pairs of forcing conditions ($f_{\text{mot}}, S_{\text{mot}}$). As shown in Fig. 8(a), the amplitude of the wave measured by the receiver decreases with increasing driving intensity, indicating a progressive rise of the mean vortex line density of the flow. Short-term fluctuations and long-term trends are also observed.

As already mentioned, these amplitude variations are not solely caused by fluctuations in vortex line density but are also influenced by temperature drifts. Fig. 8(b) shows trajectories of the complex amplitude $\tilde{U}(t)$ in polar coordinates. We observe that the complex amplitude trajectories move along both the pseudo-diameter, which correlates with damping fluctuations (i.e. vortex density changes), and the quasi-circle, which corresponds to phase shifts (i.e. second sound velocity c_2 fluctuations due to temperature changes).

Figure 8(c) shows the deduced mean vortex line density \mathcal{L} , obtained using the two methods presented in Sec. III B 1, illustrating the importance of addressing phase-shift-induced temperature effects. The

solid line represents the result from demodulating both the amplitude $U(t)$ and phase $\theta(t)$ [as described in Eqs. (13) and (14)], while the dashed line corresponds to demodulating only the amplitude $U(t)$ [as given by Eq. (11)]. Note that we take into account both the frequency and temperature dependence of the B parameter, extracted from Ref. [52]. Specifically, we use $B = 1.18$ to demodulate the measurements at $T = 2$ K and $f = 7440$ Hz (as the ones shown in Fig. 8), and $B = 1.29$ for the dataset acquired at $T = 1.6$ K and $f = 7470$ Hz.

For each forcing condition, we observe that the solid-line signals clearly stabilize at a mean value (represented by a black dotted line) after a brief transient period of a few tens of seconds (appearing as “tails” behind the point cluster in Fig. 8(b)). This confirms the stationarity of the flow and confirms that the vortex tangle densifies as the driving intensity increases.

In contrast, the dotted signals of $\mathcal{L}(t)$ are clearly affected by large temperature-induced drifts that occur when the forcing conditions change and gradually diminish as the pressure controller compensates for dissipation changes.

Finally, we observe that the different point clusters in Fig. 8(b), each associated with a given forcing, are not centered at the same phase. This is likely due to pressure sensor uncertainty : the pressure controller adjusts the aperture of the pumping valve according to the dissipated power, with final bath pressure being inside a dead band associated with pressure sensor accuracy [53].

Nevertheless, all of these considerations have demonstrated our ability to measure the mean vortex line density of the flow for different forcing conditions. Combined with the particle trajectories, we now have all the ingredients necessary to characterize the turbulent properties of the flow.

IV. LARGE-SCALE TURBULENT PROPERTIES OF THE FLOW FROM PARTICLE TRAJECTORIES

In this section, we present a detailed analysis of the particle velocities that gives us access to the large-scale properties of the flow, specifically the velocity fluctuations u_{rms} , the energy dissipation rate ϵ , and the associated integral length scale $L = u_{\text{rms}}^3/\epsilon$. We first examine the particle velocity distributions and characterize the evolution of the standard deviation u_{rms} , as a function of the forcing parameters f_{mot} and S_{mot} . Next, we turn to the characterization of the energy injection rate ϵ based on the study of the pseudo-eulerian structure functions of order 2 and 3.

A. Velocity distributions and turbulent velocity fluctuations

1. Velocity distributions

In the following, we analyze the extensive dataset obtained from the 2×2D system, which includes measurements at three different temperatures: 1.6 K (He II), 2 K (He II), and 2.3 K (subcooled He I at 100 mbar). The aim is to investigate the velocity distributions of the particles and to explore the dependence of their associated standard deviation, u_{rms} , on the forcing parameters f_{mot} and S_{mot} .

The definition of particles velocities from their trajectories, which fundamentally involves selecting a method to differentiate a discrete and noisy signal, must be approached with caution to avoid amplifying noise. In our case, we opt for a simpler and more computationally efficient approach: convolving each trajectory with a Gaussian derivative kernel, as described in Ref. [54]. To determine the appropriate Gaussian kernel size, we analyze the power spectral density of the particle trajectories, which reveals that the noise becomes significant around ~ 70 Hz. We thus select a conservative kernel width of $n_f = 15$ time steps, or $\tau_f = 5$ ms (corresponding to a characteristic frequency of ~ 200 Hz). Note that we verify that any kernel width within the range 3 to 15 time steps leads to similar values of the standard deviation of the velocity (less than 5% difference).

After computing the particle velocities, additional steps are required to isolate the velocity fluctuations induced by the turbulence. In particular, parasitic oscillations are observed in the ~ 30 -60 Hz

range, likely caused by mechanical vibrations, in some cases. These artifacts, where all particles oscillate in phase, can be mitigated by calculating the mean particle velocity frame by frame and subtracting its quasi-periodic fluctuating component from the individual trajectories.

Furthermore, preliminary analysis of the 3D dataset revealed the presence of stationary but inhomogeneous mean recirculating flow. To isolate the turbulence-induced fluctuations generated by the oscillating grids, this mean flow must also be subtracted. The detailed procedure for this critical step is provided in appendix A, covering both the 2×2D and 3D trajectories.

After completing these preprocessing steps, we can confidently analyze the velocity distributions of the particles. Given that the vertical component of particle velocities is affected by their settling velocity, which varies due to differences in particle size and density, our analysis focuses exclusively on the horizontal velocity components.

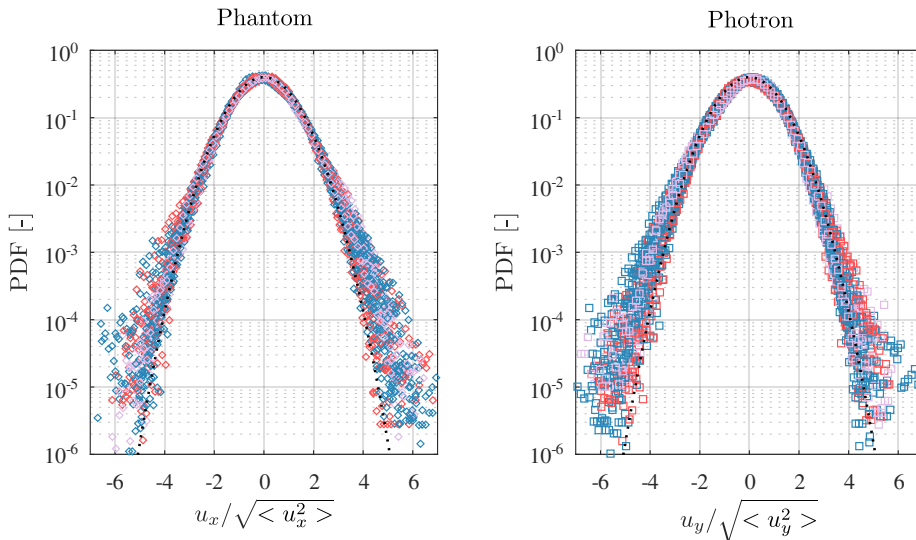


FIG. 9. Distributions of horizontal velocities normalized by their standard deviation. The means are not subtracted as they are nearly zero (never more than 3% of the corresponding standard deviation). The color code corresponds to the bath conditions: red for subcooled He I, blue for saturated He II at 2 K, and purple for saturated He II at 1.6 K. Black dotted lines represent a Gaussian distribution. (a) Velocity distribution from the horizontal component of particle trajectories obtained from Phantom camera images. (b) Same but from Photron camera images.

Figure 9 shows the horizontal velocity distributions, normalized by their respective standard deviation. The results indicate that, under this coflow configuration and across all three temperatures, the particle velocity distributions are quasi-Gaussian, in accordance with previous studies [55, 56]. Reducing the size of the differentiation kernel tends to produce larger tails and increase the flatness $F = \langle u^4 \rangle / \langle u^2 \rangle^2$, especially for low velocities, from $F \approx 4$ for the base 15 time steps kernel to 4.5 for a 3 time steps kernel. This is interpreted as a consequence of artifacts occurring during the trajectories reconstruction. Whatever the kernel size, no distinction in the shape of the velocity distributions is observed between He I and He II.

2. Turbulent velocity fluctuations

We now characterize the dependence of the velocity standard deviation, u_{rms} on the forcing parameters: the stroke S_{mot} and the oscillation frequency f_{mot} of the grids. We first examine the dependence of u_{rms} on S_{mot} for a fixed f_{mot} . Figure 10(a) shows the data obtained for a variation of S_{mot} between 12 and 30 mm for three different frequencies f_{mot} : 5, 6, and 8 Hz. Despite some scatter, a general

trend emerges from which a power law, $u_{\text{rms}} \propto S_{\text{mot}}^{1.8 \pm 0.2}$, can be reasonably extracted.

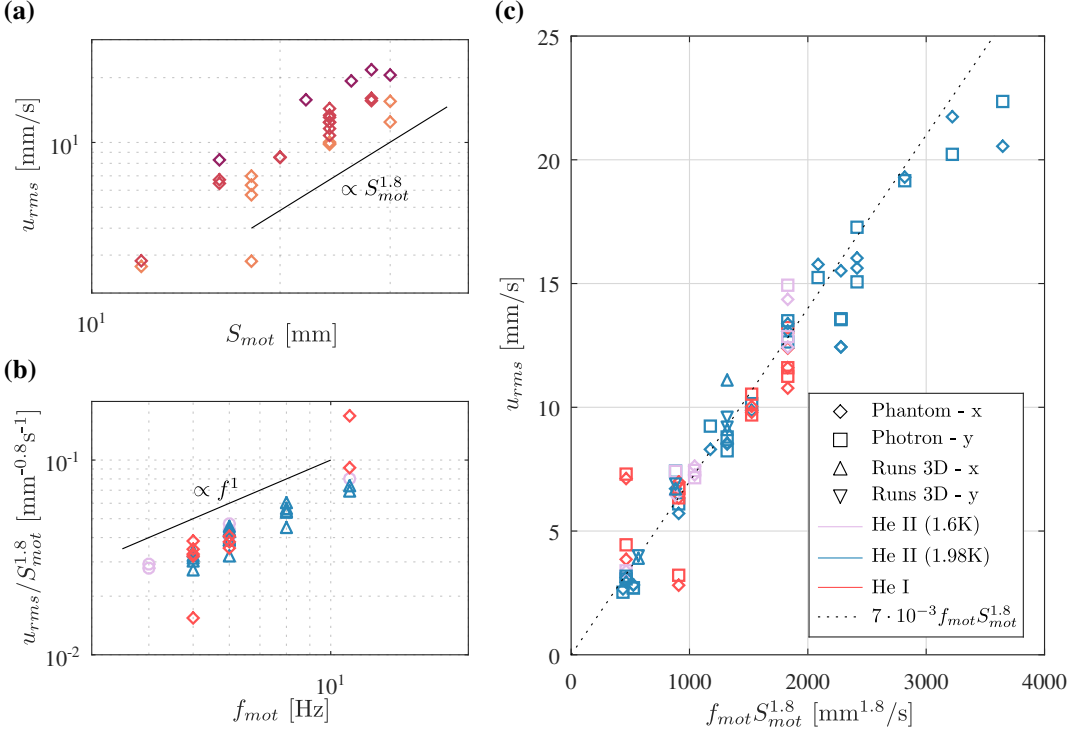


FIG. 10. Raw results showing the dependence of the velocity fluctuation standard deviation u_{rms} on the flow forcing parameters (f_{mot} , S_{mot}). Square markers represent the horizontal velocity standard deviation measured from Phantom camera images, while diamond markers correspond to measurements from Photron camera images. (a) u_{rms} as a function of S_{mot} at fixed f_{mot} . Each of the three frequencies is represented by a different color: 5 Hz (orange), 6 Hz (pink), and 8 Hz (purple). (b) $u_{\text{rms}}/S_{\text{mot}}^{1.8}$ as a function of f_{mot} . The color code indicates the bath conditions: subcooled He I (red), saturated He II at 2 K (blue), and saturated He II at 1.6 K (purple). (c) u_{rms} as a function of $f_{\text{mot}}S_{\text{mot}}^{1.8}$. The color code is the same as in (b).

Having insufficient data to perform a similar analysis of the dependence of u_{rms} on f_{mot} for fixed S_{mot} , Fig. 10(b) shows the evolution of $u_{\text{rms}}/S_{\text{mot}}^{1.8}$ as a function of frequency f_{mot} . Despite the scatter, this representation suggests that $u_{\text{rms}} \propto f_{\text{mot}}^{1 \pm 0.1}$.

Finally, to provide an overall view of the combined dependence on these two parameters, Fig. 10(c) shows u_{rms} as a function of the product $f_{\text{mot}}S_{\text{mot}}^{1.8}$. The data seem to be well aligned, and no significant difference is observed between He I/He II. These observations suggest that, within the explored parameter range, a reasonable approximation for u_{rms} can be written as:

$$u_{\text{rms}} = \gamma f_{\text{mot}} S_{\text{mot}}^{1.8} \quad (15)$$

where the prefactor $\gamma = 7 \times 10^{-3} \text{ mm}^{-0.8}$.

Given the scatter in the data, slight adjustments to the exponents could have been plausible. However, we will show that this scaling is well supported by theoretical arguments. Matsunaga *et al.* [57] applied the k - ϵ turbulence model to describe the flow generated by a single oscillating grid. Their derivation of an analytical expression for the decay of kinetic energy, $k(z) = \frac{1}{2} u_{\text{rms}}^2(z)$, as a function of the distance z from the grid, showed good agreement with experimental data available at the time [58–60], and this result has since been further validated by more recent studies (e.g., Ref. [61]).

The reported solution for the kinetic energy is given by:

$$k = k_0 \left(1 + \frac{z}{1.82L_0} \right)^{-5}, \quad (16)$$

where $L_0 = \frac{k_0^{3/2}}{\epsilon_0}$, k_0 and ϵ_0 represent respectively the integral scale, the kinetic energy, and the dissipation rate at the grid level. The values of k_0 and ϵ_0 are empirically determined based on experimental data, leading to:

$$\begin{cases} k_0 = 0.6 \left(\frac{S_{\text{mot}}}{M} \right)^{1/4} f_{\text{mot}}^2 S_{\text{mot}}^2, \\ \epsilon_0 = 0.45 \frac{S_{\text{mot}}}{M} f_{\text{mot}}^3 S_{\text{mot}}^2, \end{cases} \quad (17)$$

where M is the grid mesh size. These relations are valid for $Re_g \geq 5.5 \times 10^3$, where Re_g is the Reynolds number calculated from the grid forcing properties:

$$Re_g = \frac{f_{\text{mot}} S_{\text{mot}}^2}{\nu}.$$

Note that, although the viscosity ν of He II cannot be precisely defined for this calculation, it can be unambiguously computed for the He I runs, yielding a minimum value of $Re_g \approx 3.5 \times 10^4$. It thus seems reasonable to assume that $Re_g \geq 5.5 \times 10^3$ holds for all tested $(S_{\text{mot}}, f_{\text{mot}})$ parameter pairs in both He I and He II. It follows that $L_0 = \frac{0.6^{3/2}}{0.45} M^{5/8} S_{\text{mot}}^{3/8}$, which implies, based on Eq. (16), that the dependence of u_{rms} on the stroke S_{mot} does not follow a simple power-law behavior:

$$u_{\text{rms}} \approx 0.8 f_{\text{mot}} M^{1/8} S_{\text{mot}}^{9/8} \left(1 + \frac{z}{1.9 M^{5/8} S_{\text{mot}}^{3/8}} \right)^{-5/2}.$$

In our parameter range, at the mid-plane between the two grids, $z = H/2$, this analytical relation can be approximated by the following power law,

$$u_{\text{rms}} \propto f_{\text{mot}} S_{\text{mot}}^{1.82},$$

which corroborates Eq. (15) established from the raw data and gives an explanation for the somewhat unintuitive $u_{\text{rms}} \propto S_{\text{mot}}^{1.8}$ scaling.

B. Injected energy at large scales

In classical homogeneous and isotropic turbulence, the exact $\frac{4}{5}$ -th law states (see, e.g., Pope [62], page 204), for scales r within the inertial range, that the third-order longitudinal structure function is expressed as

$$S_{3,\parallel} = \langle (\delta_r u_{\parallel})^3 \rangle = -\frac{4}{5} \epsilon r. \quad (18)$$

This law could thus be used as a tool to estimate ϵ , the energy transfer rate across scales in the inertial range, using distributions of longitudinal velocity increments computed for various scales r within the inertial range. This energy transfer rate is interpreted, given the stationarity of the flow, as the flux of energy injected at large scales and dissipated at small scales. It is known that the $\frac{4}{5}$ -th law holds in

He II, at least in the upper part of the inertial range [22], and that, under identical forcing, the energy injection rate and, thus, the dissipation rate in He I and He II are the same [18].

In classical turbulence, the large-scale energy injection rate can be written (see, e.g., Pope [62], p. 244) as

$$\epsilon = \frac{u_{\text{rms}}^3}{L}. \quad (19)$$

Thus, in what follows, we aim to use the $\frac{4}{5}$ -th law to estimate ϵ and deduce the value of the integral scale L from Eq. (19).

Due to the indeterminacy of particle positions in the depth of the camera fields of view, 2×2D measurements cannot be used to compute 1 longitudinal velocity increments. This can be achieved using the 3D measurements though. By denoting $\mathbf{v}(\mathbf{P}^i(t_k), t_k)$ the velocity of the i -th particle at position $\mathbf{P}^i(t_k)$ at time t_k , we can define the set of longitudinal velocity increments at scale r and time t_k as follows:

$$\{\delta_r u_{\parallel}(t_k)\} = \left\{ \left[\mathbf{v}(\mathbf{P}^i(t_k), t_k) - \mathbf{v}(\mathbf{P}^j(t_k), t_k) \right] \cdot \mathbf{e}^{ij} \right\}_{\{i,j\} \text{ such that } ||\mathbf{P}^i \mathbf{P}^j(t_k)|| \in \Omega_r}, \quad (20)$$

where $\mathbf{e}^{ij} = \frac{\mathbf{P}^i \mathbf{P}^j(t_k)}{||\mathbf{P}^i \mathbf{P}^j(t_k)||}$ and $\{\cdot\}_{\{i,j\} \text{ such that } ||\mathbf{P}^i \mathbf{P}^j(t_k)|| \in \Omega_r}$ denote the set of particle pairs $\{i, j\}$ whose separation distance $||\mathbf{P}^i \mathbf{P}^j||$ at time t_k is within the interval Ω_r . The total distance between the two particles, to which we do not have access in 2×2D measurements, is therefore essential for calculating longitudinal increments. This approach is referred to as “pseudo-Eulerian” because each particle is considered a velocity sensor in the flow. Note that the particle velocities along their 3D trajectories were computed using the same method described earlier for the 2×2D data in Sec. IV A, employing an adjusted kernel width of four images, corresponding to approximately $\tau_f = 20$ ms.

By combining values across different instants, the longitudinal structure functions of order $p \in \mathbb{N}$ can be defined as:

$$S_{p,\parallel}(r) = \langle (\delta_r u_{\parallel})^p \rangle.$$

For each instant t_k of the 3D runs, we computed the velocity differences between pairs of particles and sort the results based on the distance between the pairs into intervals. Following our observations in the previous paragraphs, we aim to mitigate the effects induced by the distribution of sedimentation velocities, which manifest in the vertical component. Therefore, we restrict the calculation of longitudinal velocity increments to pairs of particles satisfying $\mathbf{e}^{ij} \cdot \mathbf{e}_z \approx 0$. This ensures that the contribution of velocity differences along the vertical component is negligible compared to those along the horizontal components. In practice, we only consider pairs whose vertical separation distance is less than 10% of their total separation distance. Figure 11 presents the distributions obtained from one of the 3D acquisitions for several intervals of distance between particle pairs.

Qualitatively, the distributions are well-converged and approximately Gaussian at large scales, while exhibiting broader tails at smaller scales, a marker of turbulence intermittency. It naturally follows to compute the third-order moment of the distributions to construct $S_{3,\parallel}(r)$, the longitudinal third-order structure function, and then the energy transfer rate ϵ following Eq. (18). In Fig. 12(a) we present the latter as a function of the considered scale r for the four 3D runs.

First, note that the curves corresponding to runs 2, 3, and 4 reveal the persistence of a large-scale bias (for $r > 20$ mm): at sufficiently large scales, a Gaussian distribution of velocity increments is expected, implying $\langle (\delta_r u_{\parallel})^3 \rangle = 0$. This behavior can most likely be attributed to a residual influence of the mean flow.

To further interpret the curves in the light of Kolmogorov’s theory at intermediate scales ($r < 20$ mm), it is essential to caution the reader. In practice, the $\frac{4}{5}$ -law is strictly valid in the inertial range only if the Kolmogorov cascade depth is sufficient, meaning the ratio between the forcing scale L and the dissipative scale η is large enough. According to the investigations of Moisy *et al.* [63], to observe

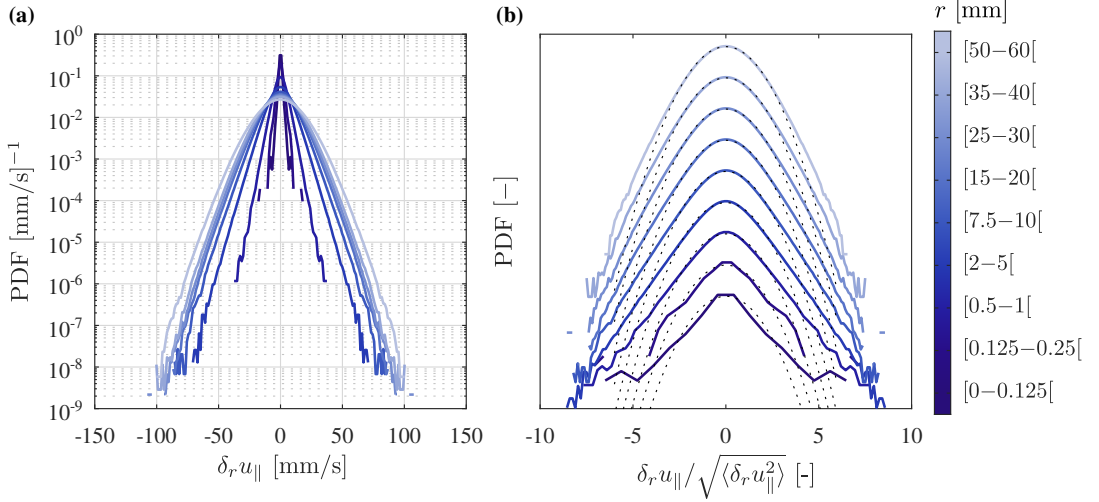


FIG. 11. a) Distribution of velocity increments $\delta_r u_{||}$ for several intervals of distance between particles for the run 3D-2 (He II at 2 K). The four smallest intervals (one of which is not shown to avoid overloading the graph) of inter-particle distances below 1 mm contain respectively 730, 4200, 38000, and 350000 pairs. The others contain more than a million pairs. b) The same distributions normalized by their standard deviation and arbitrarily shifted on the vertical axis.

an unambiguous plateau in the representation of $|S_{3,||}(r)| / \left(\frac{4}{5}r\right)$, whose height can be interpreted as ϵ , the scale-separation condition must satisfy $L/\eta \gtrsim 4000$ (or equivalently $\text{Re}_\lambda \gtrsim 1000$). If this condition is not met, the expected shape is rather a bell-curve, whose maximum should be interpreted as $\gamma\epsilon$, where $\gamma \leq 1$ is a coefficient that increases with the cascade depth for which the authors propose the following expression:

$$\gamma \approx 1 - 12 \left(\frac{L}{\eta}\right)^{-4/5}. \quad (21)$$

Finally, note that the position r_{max} of this maximum also depends on the cascade depth, and r_{max} is expected to decrease as the ratio L/η becomes smaller.

The experimental results in Fig. 12(a) appear to align with these considerations, suggesting that the scale separation is insufficient to clearly observe a plateau. The maximum of the curves in Fig. 12(b) should therefore be interpreted as $\gamma\epsilon$ and not directly as ϵ . However, estimating the value of γ at this stage is delicate because we lack estimates of both the integral scale L and the dissipative scale η . Temporarily assuming that the scale separation is sufficient to consider $\gamma \approx 1$, the validity of this assumption will be verified *a posteriori*.

From the measurement of the bell-curve maxima, we thus obtain an estimate of the energy dissipation rate ϵ . Combined with u_{rms} , this allows us to estimate L , the integral scale of the flow, from Eq. (19). Note that, instead of using Eq. (15) to compute u_{rms} , we directly measured the standard deviation of the particle velocities in the two horizontal components, $u_{\text{rms},x}$ and $u_{\text{rms},y}$, and took their mean. The resulting values are reported in Table I.

Given the sensitivity of this method for estimating the integral scale L to small inaccuracies in the velocity root mean square [it is raised to the power of 3 in Eq. (19)], the obtained values appear consistent overall. The mean value, $L = 16$ mm, thus serves as a first good estimate.

We can now try to check the validity of the assumption regarding the value of $\gamma \approx 1$. In the absence of a better approach, we can use the results of classical turbulence theory to roughly estimate the dissipative scale, $\eta = (\nu^3/\epsilon)^{1/4}$, where $\nu = \mu/\rho$ is the kinematic viscosity calculated from the dynamic viscosity of the normal component and the total density $\rho = \rho_s + \rho_n$.

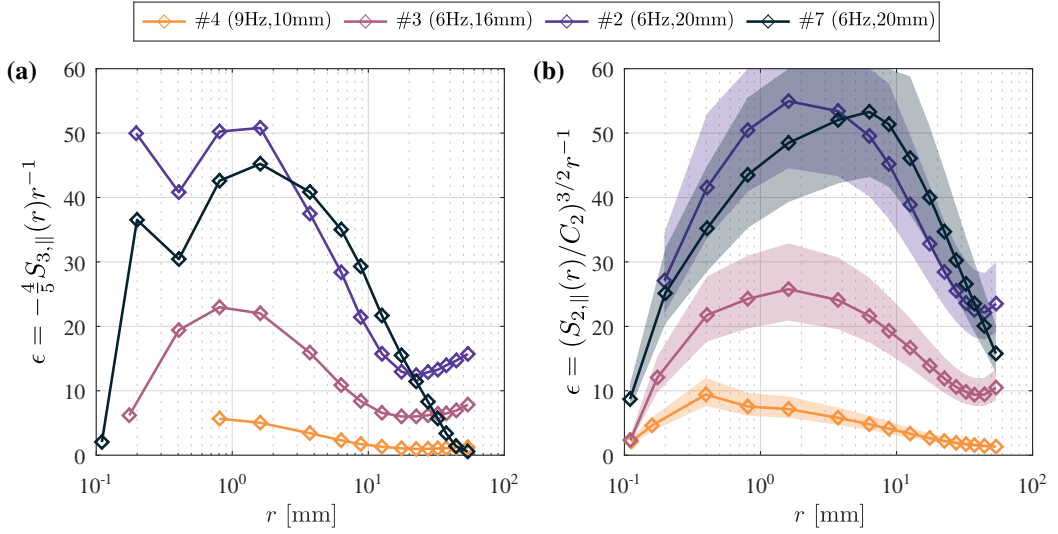


FIG. 12. a) Pseudo-Eulerian third-order longitudinal structure function of particle velocity $S_{3,\parallel}$, derived from the 3D dataset (He II at 2 K) with run IDs referenced in the legend as #n, compensated as suggested by Eq. (18) to directly read ϵ from the maximum of the bell-curves maxima. To avoid biased interpretations, the marker positions on the abscissa correspond to the average distance between particle pairs within each interval, ensuring consistency even when the inter-particle distance distribution is non-uniform. Note that certain points at the smallest scales are excluded (for $r < 0.125$ mm for runs 2 and 3, and all points for $r < 0.5$ mm for run 4), where we measure $S_{r,\parallel} > 0$. b) Pseudo-Eulerian second-order longitudinal structure function of particle velocity $S_{2,\parallel}$, derived from the 3D dataset (He II at 2 K). To allow direct comparison with the ϵ value deduced from part a), the curves are compensated as suggested by Eq. (22). The shaded area represents the uncertainty on the value of $C_2 \in [1.7-2.3]$.

Run	Forcing	u_{rms} [mm/s]	ϵ_{S_3} [mm ² /s ³]	L [mm]	$\epsilon_{S_3}^*$ [mm ² /s ³]	L^* [mm]	ϵ_{S_2} [mm ² /s ³]
2	(6Hz,20mm)	9.2	50.8	15.3	52.9	14.7	44.6-70.1
3	(6Hz,16mm)	6.8	23	13.7	24.2	13	20.9-32.9
4	(9Hz,10mm)	3.9	5.7	10.4	6.2	9.5	5.9 - 9.3
7	(6Hz,20mm)	10.4	45.2	24.9	46.5	24.2	43.2 - 68

TABLE I. Estimation of the energy injection rate ϵ and the integral scale L based on the 3D dataset (He II at 2 K). The values ϵ^* and L^* are the corrected estimates of ϵ and L to account for the finite depth of the Kolmogorov cascade.

It follows that, for the four 3D runs, $L/\eta > 700$, and thus, according to Eq. (21), $\gamma > 0.93$. Considering the measurement uncertainties, the approximation $\gamma \approx 1$ appears relatively reasonable and leads to only a marginal underestimation of ϵ . More quantitatively, assuming that this method of estimating γ is valid in He II, the procedure can be iterated until convergence of the γ value is achieved for each of the four runs. The updated values $\epsilon_{S_3}^*$ and the associated L^* are reported in table I.

The new mean value of the integral scale is then marginally different, $L = 15.3 \pm 6$ mm.

To further validate the integral scale estimation via the $\frac{4}{5}$ -law, we also analyze the second-order moments of longitudinal velocity increments. According to classical turbulence theory, the second-order longitudinal structure function for scales r in the inertial range is expressed as:

$$S_{2,\parallel}(r) = C_2 \epsilon^{2/3} r^{2/3} \quad (22)$$

where $C_2 \in [1.7-2.3]$ (see, e.g., Pope [62], p. 193–194). This provides another method to estimate ϵ

using the $r^{2/3}$ scaling regime in the inertial range.

As illustrated in Fig. 12(b), the expected inertial range regime is well-defined, extending down to the smallest well-resolved scales of approximately $\sim 200\text{--}400\text{ }\mu\text{m}$. By defining the plateau height on the log-log graph of $(S_{2,\parallel}/C_2)^{3/2}/r$ (Fig. 12(b)) as ϵ , we thus define ϵ_{S_2} for $C_2 = 1.7$ and $C_2 = 2.3$ to capture the range of uncertainty.

Both approaches, using S_3 and S_2 , show good agreement given the difficulty of such measurement. These results thus confirm the validity of the $\frac{4}{5}$ -law approach for estimating ϵ and give credit to the associated integral scale value, $L = 15.3 \pm 6\text{ mm}$.

Combined with Eq. (15), which estimates u_{rms} , this value of L enables the estimation of the energy dissipation rate $\epsilon = u_{\text{rms}}^3/L$ for any pair of forcing parameters $(f_{\text{mot}}, S_{\text{mot}})$. This provides a complete description of the large-scale properties of the flow.

V. EFFECTIVE VISCOSITY OF QUANTUM TURBULENCE

A. Experimental results of the mean vortex line density

After applying the calibration protocol proposed in Sec. III B 3 to properly interpret the second sound signals in the phase/amplitude space both at 30.0 mbar (2 K), and at 7.5 mbar (1.6 K), we gathered a database of signals spanning a wide range of flow forcings, from $u_{\text{rms}} \approx 0.5\text{ mm/s}$ to $u_{\text{rms}} \approx 20\text{ mm/s}$. Each measurement series, in which the motor frequency f_{mot} was varied at fixed amplitude or vice versa, was processed in a manner similar to the previous example to deduce the average vortex line density of the flow.

As with the turbulent velocity fluctuations u_{rms} , we then investigated the possibility of extracting power laws. Figure 13(a) presents the dependence of the mean vortex line density on f_{mot} , varied from 2 to 11 Hz, for four different strokes S_{mot} : 8, 16, 22, and 28 mm. The data suggest a scaling of $\mathcal{L} \propto f_{\text{mot}}^{1.5}$. Similarly, Fig. 13(b) shows \mathcal{L} as a function of S_{mot} , varied from 4 to 32 mm, for four different motor frequencies f_{mot} : 3, 6, 7, and 9 Hz, yielding $\mathcal{L} \propto S_{\text{mot}}^{2.7}$.

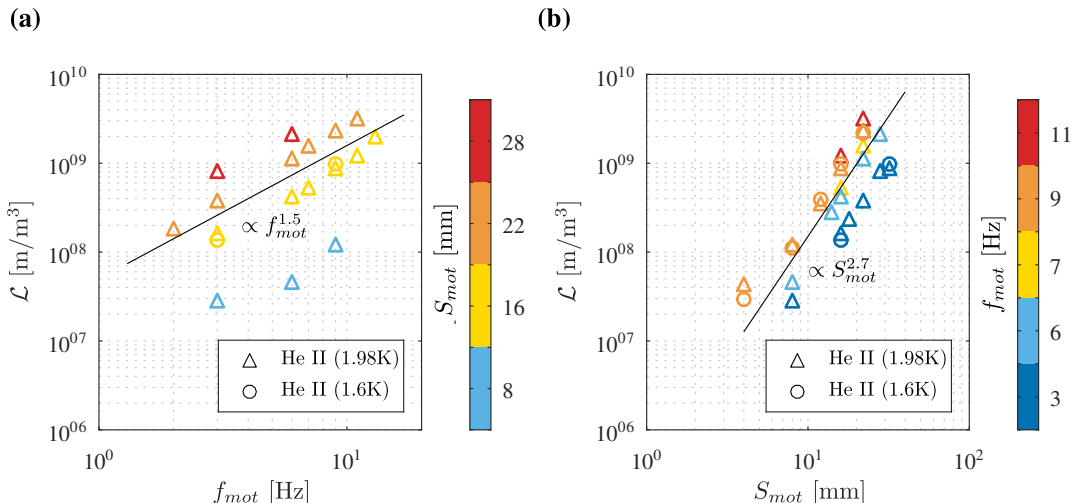


FIG. 13. Raw results showing the dependence of the mean vortex line density \mathcal{L} on the flow forcing parameters $(f_{\text{mot}}, S_{\text{mot}})$. The two symbol shapes indicate the two temperatures (\circ 1.6 K, \triangle 2 K). (a) \mathcal{L} as a function of f_{mot} at fixed strokes $S_{\text{mot}} = 8\text{ mm}, 16\text{ mm}, 22\text{ mm}, 28\text{ mm}$. (b) \mathcal{L} as a function of S_{mot} at fixed frequencies $f_{\text{mot}} = 3\text{ Hz}, 6\text{ Hz}, 7\text{ Hz}, 9\text{ Hz}$.

Recalling the scaling Eq. (15) established in Sec. IV A 2, $u_{\text{rms}} \propto f_{\text{mot}}^{1.8} S_{\text{mot}}^{1.8}$, the observed scaling

$\mathcal{L} \propto f_{\text{mot}}^{1.5} S_{\text{mot}}^{2.7}$ clearly suggests $\mathcal{L} \propto u_{\text{rms}}^{3/2}$. Obviously, exponents could be subject to slight adjustments, especially since the $u_{\text{rms}} \propto f_{\text{mot}} S_{\text{mot}}^{1.8}$ scaling may represent only a local trend, given that the broader Eq. (15) derived from the k - ϵ model cannot be expressed as a pure power law (see Sec. IV A 2).

B. Estimation of ν_{eff} and comparison with literature

Figure 14 presents all results obtained at 2 K and 1.6 K. To aid interpretation, the data are displayed from two perspectives. In Fig. 14(a), we plot the mean inter-vortex distance, $\ell = 1/\sqrt{\mathcal{L}}$, in the range $15 \mu\text{m} \lesssim \ell \lesssim 150 \mu\text{m}$, normalized by the integral length scale L , as a function of the Reynolds number, $\text{Re}_\kappa = u_{\text{rms}} L / \kappa$. Figure 14(b) shows the dissipation rate, $\epsilon = u_{\text{rms}}^3 / L$, as a function of $(\kappa \mathcal{L})$.

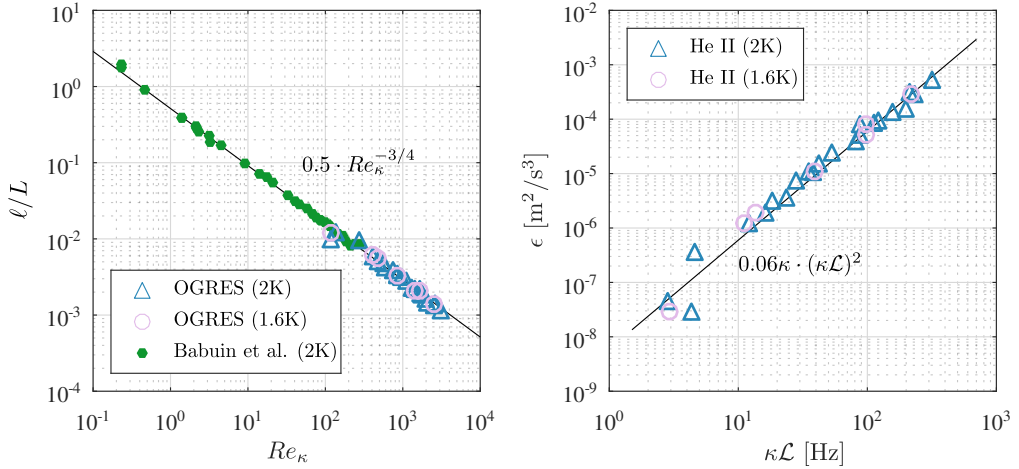


FIG. 14. Compilation of second sound measurements. Blue markers correspond to measurements at 2 K, while purple markers correspond to 1.6 K at saturation. Green markers show data retrieved from Ref. [32], for comparison. (a) Mean inter-vortex distance, $\ell = 1/\sqrt{\mathcal{L}}$, normalized by the integral scale L , as a function of the Reynolds number, $\text{Re}_\kappa = u_{\text{rms}} L / \kappa$. (b) Dissipation rate, $\epsilon = u_{\text{rms}}^3 / L$, plotted against $(\kappa \mathcal{L})$.

Our measurements at both 1.6 K and 2 K clearly suggest that

$$\epsilon \approx 0.06\kappa(\kappa\mathcal{L})^2. \quad (23)$$

This scaling is consistent with Eq. (1) from which we extract $\nu_{\text{eff}} \approx 0.06\kappa$, or more precisely by fitting the data:

$$\nu_{\text{eff}}(T = 1.6 \text{ K}) = 0.061\kappa, \quad \nu_{\text{eff}}(T = 2 \text{ K}) = 0.054\kappa. \quad (24)$$

As we saw that Eq. (1) is equivalent to Eq. (3) and it is useful to translate these ν_{eff} values in terms of $\beta = (\nu_{\text{eff}}/\kappa)^{1/4}$:

$$\beta_{\text{exp}}(T = 1.6 \text{ K}) = 0.5, \quad \beta_{\text{exp}}(T = 2 \text{ K}) = 0.48. \quad (25)$$

We can now compare our results with those of Babuin *et al.* [32], which also come from a steady-state turbulent flow. Their data for ℓ/L at 1.95 K (retrieved manually and plotted in Fig. 14(a)) show excellent agreement with our measurements. This reinforces the robustness of the remarkable reported value $\beta \approx 0.5$ from Salort *et al.* [24], which combines numerical simulations and a compilation of values extracted from previously published studies in pipe flows [64–66].

To further explore the comparison of our data with the one obtained by Babuin *et al.* [32], Fig. 15 presents their values of ν_{eff} for various temperatures alongside our estimates. Since $\nu_{\text{eff}} \propto \beta^4$, even minor discrepancies in β are amplified in this representation.

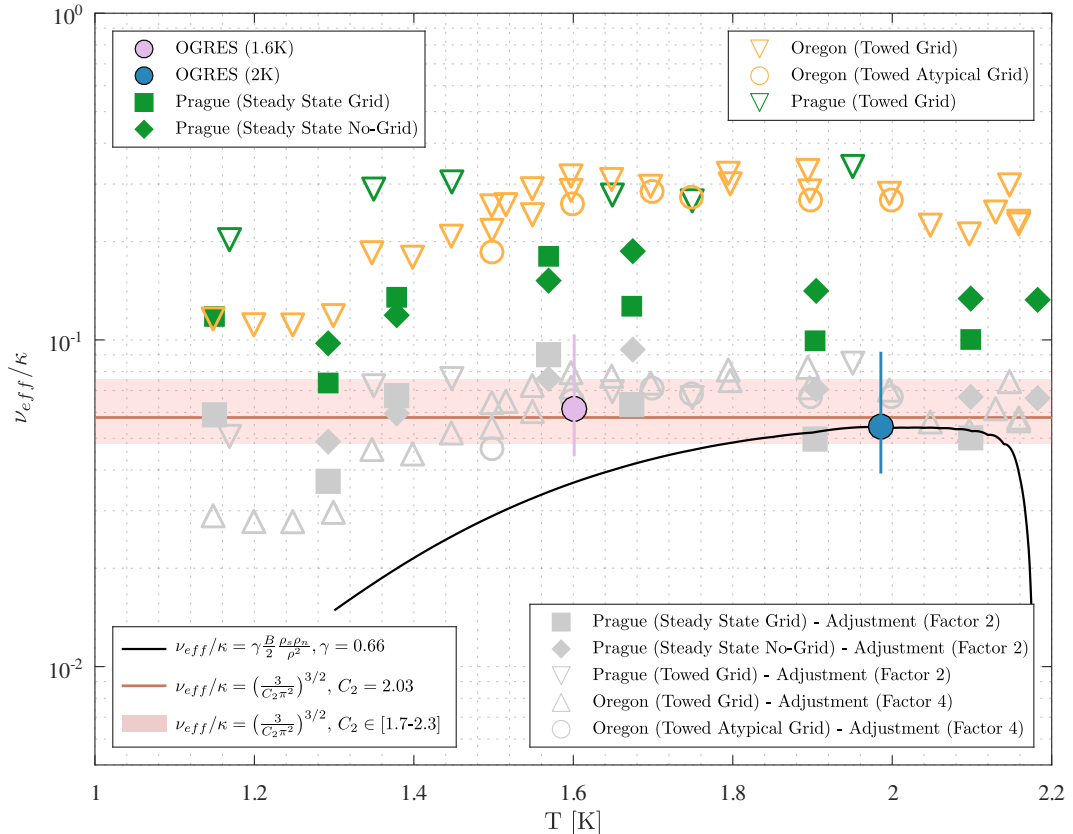


FIG. 15. Compilation of effective viscosity ν_{eff} values as a function of temperature. Our measurements are plotted alongside previous experimental datasets from Prague (Towed Grid [30], Grid and No-Grid Steady State [32]) and Oregon (Towed Atypical Grid [28] and Towed Grid [29]). Note that the Oregon data were corrected by a factor $(3\pi/8)^2$ to account for the sine-squared dependence, as discussed in [67]. Also shown are the predicted values of ν_{eff} from Eq. (5) for $\gamma = 0.66$ (in black), and from Eq. (29) (in red).

Babuin *et al.* [32] carefully analyzed their results and estimated the uncertainty on the value of ν_{eff} to be of the order of ten (temperature independent), mainly due to their indirect estimation of large-scale flow properties. As shown gray in Fig. 15, with an arbitrary adjustment of a factor of 2, their two steady-state datasets (solid markers) are in excellent agreement with our measurements. Following their approach, we also plotted the relation of Eq. (5), which predicts the temperature dependence of ν_{eff} assuming that dissipation is entirely due to mutual friction (we adjusted the parameter $\gamma = 0.66$ to match our measurements at 2 K). As in Babuin *et al.* [32] measurements, where the temperature likely reflects experimental noise, our measurements suggest that if a dependence exists, it must be very weak resulting in a poor agreement of Eq. (5) with the measurements. Therefore and as it is discussed in section VI, it seems very unlikely that mutual friction is responsible for 100% of the dissipation in the explored temperature range.

Finally, we also include the available decaying datasets from Stalp *et al.* [28], Niemela *et al.* [29], and Babuin *et al.* [30]. As explained in Sec. I, a key step in determining the ν_{eff} value from these

experiments is assuming that the integral scale L saturates at the channel diameter D . If we adjust this assumption to consider that it saturates at the channel radius $D/2$, v_{eff} is corrected by a factor of 4. The corrected data (in grey in Fig. 15) align quite well with our measurements.

To conclude, since we have unambiguously characterized ϵ using particle velocity measurements – something that, to our knowledge, had never been done before – we can reasonably consider our values to be the best current estimates.

VI. INTERPRETATION OF THE KOLMOGOROV-LIKE SCALING

As pointed out by Babuin *et al.* [32], although the scaling expressed in Eq. (1) – or equivalently Eq. (3) – has been experimentally observed numerous times across different temperatures and appears remarkably robust, it still lacks a rigorous theoretical justification. Phenomenologically, the introduction of the “effective viscosity” v_{eff} is motivated by analogy with the classical expression $\epsilon = \nu \langle \omega^2 \rangle$. This suggests that ℓ represents the characteristic scale of a non-viscous dissipation process, namely *mutual friction*. However, as shown on Fig. 15, most available data (including our own) in the 1–2.17 K temperature range are incompatible with a scenario in which all dissipation arises solely from mutual friction.

In this section, we aim to revisit a prescient argument proposed by Vinen [68], which, despite its potential, does not seem to have led to the conclusive consensus it arguably merits.

The idea is conceptually straightforward, arising from classical considerations of velocity fields in homogeneous and isotropic turbulence within the inertial range of scales, bounded by the dissipation scale η (whatever the underlying dissipation mechanism) and the integral scale L , i.e. $\eta \ll r \ll L$. To begin with, we recall that the characteristic circulation $\Gamma(r)$ around a loop C of diameter r within this range of scales is prescribed by Kolmogorov’s 1941 (K41) theory (see Ref. [69] for a detailed discussion on the applicability of K41 in estimating $\Gamma(r)$), and can be written as:

$$\Gamma(r) = \oint_C \mathbf{v} \cdot d\mathbf{l} = \pi r \frac{\delta_r v_{\perp}}{2}. \quad (26)$$

Since r lies within the inertial range of scales, the transverse velocity increment $\delta_r v_{\perp}$ can be estimated as (see, for example, Pope [62], pp. 193–194):

$$(\delta_r v_{\perp})^2 = \frac{4}{3} (\delta_r v_{\parallel})^2 = \frac{4}{3} C_2 (\epsilon r)^{2/3},$$

Therefore, the circulation around any loop C of diameter r becomes:

$$\Gamma(r) = \sqrt{\frac{C_2 \pi^2}{3}} \epsilon^{1/3} r^{4/3}, \quad (27)$$

and the intervortex distance ℓ_{K41} , has to satisfy $\Gamma(\ell_{K41}) = \kappa$, yielding

$$\ell_{K41} = \left(\frac{3}{C_2 \pi^2} \right)^{3/8} \left(\frac{\kappa^3}{\epsilon} \right)^{1/4}. \quad (28)$$

Using the relation $\epsilon = u_{\text{rms}}^3 / L$, we can rewrite Eq. (28) in the same form as Eq. (3):

$$\frac{\ell_{K41}}{L} = \underbrace{\left(\frac{3}{C_2 \pi^2} \right)^{3/8}}_{\beta_{K41}} \text{Re}_{\kappa}^{-3/4}. \quad (29)$$

We thus obtain the predicted value of the prefactor β_{K41} in the classical K41 framework, which can be used to assess the validity of this interpretation. Given the range $C_2 \in [1.7, 2.3]$ reported in the literature, we find:

$$0.47 < \beta_{K41} < 0.52. \quad (30)$$

This value of β_{K41} , obtained without any adjustable parameters, is in very good agreement with the experimentally measured $\beta_{exp} \approx 0.5$ and values reported in the literature [24], yielding:

$$\ell \approx \ell_{K41} \quad (31)$$

This suggests that the Kolmogorov cascade not only describes the large-scale structure of quantum turbulence, as was already well established [20, 22], but extends all the way down to the mean intervortex scale ℓ . The temperature independence of the datasets in Fig. 15 further supports this paradigm, as

$\beta_{K41} = \left(\frac{3}{C_2\pi^2}\right)^{3/8}$ does not depend on temperature.

Pushing this interpretation further, it suggests that the effective viscosity $\nu_{eff} = \beta^4\kappa$ does not represent dissipation per se (as proposed by [32]), but instead characterizes an inertial-scale structural property of the flow.

Nevertheless, it should be noted that this argument appears to break down at very low temperatures. Even though the Kolmogorov-like scaling of Eq. (3) persists, measurements from the Manchester group indicate a reduction in β in this regime (see e.g., [31]). Identifying the temperature at which Eq. (31) ceases to be valid remains an open question for future research.

VII. CONCLUSION AND FURTHER COMMENTS

In this article, we report an experimental characterization of coflow turbulence in superfluid helium at temperatures of 1.6 and 2 K, generated by a double oscillating grid system with adjustable stroke S_{mot} and frequency f_{mot} (Sec. II). By seeding the flow with microspheres, we achieved – for the first time in such a cryogenic experiment – three-dimensional tracking of particle trajectories (Sec. III A). This allowed a direct measurement of the main flow large scale properties (Sec. IV), in particular the dependence of the intensity of velocity fluctuations u_{rms} on the forcing parameters (S_{mot}, f_{mot}) as well as the integral length scale $L = u_{rms}^3/\epsilon$ based on an estimate of ϵ through pseudo-eulerian velocity structure functions at scales larger than $L/20 \approx 1$ mm.

In parallel, we determined the mean vortex line density \mathcal{L} by measuring the attenuation of a second-sound standing wave across the flow, and, assuming smooth vortices, we inferred the corresponding intervortex spacing $\ell = 1/\sqrt{\mathcal{L}}$ (Sec. III B). Combining the two approach, our results reveal (Sec. V),

$$\frac{\ell}{L} = \beta_{exp} \text{Re}_\kappa^{-3/4}, \quad (32)$$

where $\beta_{exp} \approx 0.5$ appears to be a temperature-independent coefficient in our working temperature range (at 1.6 and 2 K). For the first time, this result is established by fully measuring the properties involved, (in particular, the estimate of the integral scale L derives from direct measurements, and not from a generic assumption).

We then attempt to interpret this result, particularly what can be learned from the absolute value of β_{exp} and its apparent lack of temperature dependence (Sec. VI).

As presciently predicted by Vinen [68], it appears that Eq. (32) is in perfect quantitative agreement with the classical scaling laws of a homogeneous and isotropic turbulent cascade: the scale ℓ_{K41} in the inertial range at which the circulation around a contour of diameter ℓ_{K41} equals κ quantitatively corresponds to the intervortex distance, $\ell \approx \ell_{K41}$, and an analytical expression for β can be derived:

$$\beta_{K41} = \left(\frac{3}{C_2\pi^2}\right)^{3/8} \approx 0.5.$$

This interpretation, asserting that classical turbulent scaling laws apply not only to the upper part of the inertial also range but down to the mean intervortex scale in quantum turbulence, is further supported by the temperature independence of β . Indeed, the fraction of total dissipation attributed to mutual friction is given by:

$$\frac{\epsilon_{mf}}{\epsilon} = \frac{B}{2} \frac{\rho_s \rho_n}{\rho^2} \frac{\gamma}{\beta^4}. \quad (33)$$

In the scenario proposed by Babuin *et al.* [32], where all dissipation is attributed to mutual friction ($\epsilon_{mf} \sim \epsilon$), Eq. (33) implies that $\beta^4 \propto \frac{B}{2} \frac{\rho_s \rho_n}{\rho^2}$, thus predicting a temperature dependence of β that we do not observe (see Fig. 15).

The coincidence in both the value and temperature independence of β_{exp} and β_{K41} strongly suggests that the traditional interpretation of the effective viscosity ν_{eff} as a manifestation of mutual friction is likely incorrect. Rather, it reflects an inertial-scale structural feature of the flow.

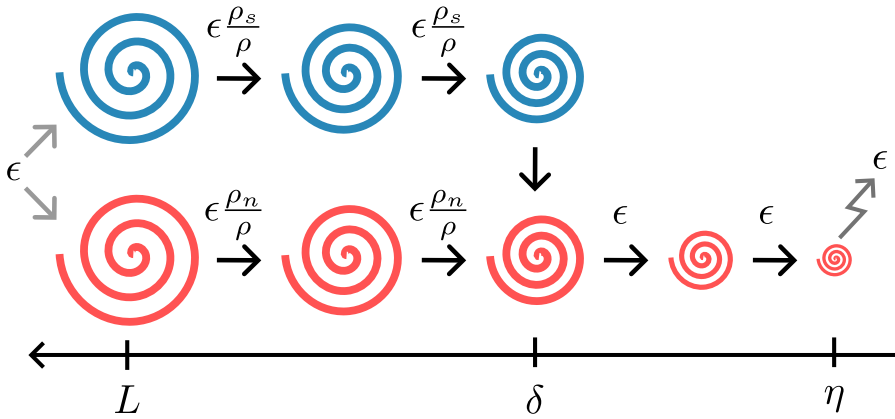


FIG. 16. Adaptation of the Richardson Cascade for Quantum Turbulence.

All of these considerations support a schematic representation of turbulent cascades in coflow experiments at $T \gtrsim 1$ K, as illustrated in Fig. 16. At large scales, energy is injected into both the normal and superfluid components, weighted by their respective densities. Classical turbulence mechanisms transfer energy down to the scale ℓ in the superfluid, and to the viscous dissipation scale η in the normal component. Mutual friction couples the two components, enabling energy exchange with negligible dissipation. The energy carried by the superfluid component is ultimately transferred and dissipated by the normal component at smaller scales, $\eta = (\nu^3/\epsilon)^{1/4}$, where $\nu = \mu/\rho$. This further implies that the counterflow velocity remains small compared to the characteristic velocity at scale ℓ , indicating that the normal and superfluid components remain locked down to that scale. This scenario is confirmed by recent results obtained using a two fluid Hall-Vinen-Bekharevich-Khalatnikov (HVBK) numerical study [70]. A more detailed discussion about the intensity of mutual friction dissipation can be found in Bret [43].

Finally, a direct trivial implication of these considerations is that for flows at $T > 1$ K – where the normal component is still present – the intervortex distance ℓ is greater than the viscous dissipation scale η , with

$$\frac{\ell}{\eta} = \beta \left(\frac{\kappa}{\nu(T)} \right)^{3/4}$$

leading to $1.4 < \ell/\eta < 3.2$.

VIII. ACKNOWLEDGMENT

The authors warmly thank Jérôme Chartier for his technical support in setting up and running the experiments. We also thank Julien Salort, Elian Bernard and Mickaël Bourgoïn from the Laboratoire de Physique de l'ENS de Lyon for lending us the MiniShaker and assisting us in its use, which enabled us to capture for the first time 3D particle trajectories in superfluid helium. We are also thankful to the members of the Nanofab team at Institut Néel, who did the Al deposits on the porous membranes of the second sound sensors. Finally we would like to thank our colleagues from the informal *TURbulent SUPERfluid GREnoble* group, and especially Juan Ignacio Polanco, Mathieu Gibert and Philippe-Emmanuel Roche, for their valuable discussions and step-by-step insights into the interpretation of our experimental results.

IX. APPENDIX

Appendix A: Mean flow correction

1. On the 3D Trajectories

A well-known challenge in oscillating grid experiments is the tendency of the flow to develop a parasitic recirculation, typically sensitive to initial conditions and exhibiting complex spatial structures [71]. In our setup, the initial conditions are inherently non-reproducible due to slight but continuous variations in the liquid level during the experiment (on the order of 1 mm/min). Moreover, we suspect that the secondary flow is further amplified by the in-phase oscillation of the grids – a constraint imposed by the cryostat geometry – which is likely less favorable than an out-of-phase configuration. The resulting mean flow often manifests as a net vertical drift of the particles, typically downward, though upward drifts are also occasionally observed.

To isolate the turbulent velocity fluctuations from the background mean flow, we apply a straightforward correction procedure. The 3D Eulerian mean velocity field $\mathbf{U}(\mathbf{x})$ is computed by discretizing the measurement volume into cubic cells of size $1 \times 1 \times 1 \text{ mm}^3$ and averaging the particle velocities of all trajectories passing through each cell over the entire duration of the run. Given the long acquisition time of our 3D experiments (over ten seconds), which greatly exceeds the turbulence integral time scale (a few seconds), the temporal averaging effectively suppresses turbulent fluctuations. As a result, to extract the turbulent velocity component of each particle along its trajectory, we simply subtract the interpolated mean flow value at the particle's position.

Figure 17 shows the resulting mean flow field for two of the 3D runs. In addition to the irreproducibility of the mean flow direction under nominally identical forcing conditions, Fig. 17 reveals substantial spatial inhomogeneities. If not subtracted, this mean flow would thus introduce a significant bias in the analysis of particle velocities.

Finally, the stationarity of the mean flow has also been verified by comparing the full-run mean field with that computed from only the first half of the acquisition.

2. On the 2×2D Trajectories

In order to suppress the recirculating flow on the 2×2D trajectories, we apply the same methodology as for the 3D measurements. The image is divided into cells of $40 \times 40 \text{ px}^2$ (roughly $0.8 \times 0.8 \text{ mm}^2$), in which we compute the average particle velocity. Since the depth of field of each camera is approximately 30 mm, the resulting mean flow corresponds to a 2D projection averaged along the optical axis. This averaging smooths out any depth-dependent inhomogeneities and may introduce a bias.

However, Fig. 17 suggests that the strongest inhomogeneities in the mean flow occur on spatial scales larger than the depth of field. The typical measurement volume for a single camera in the 2×2D

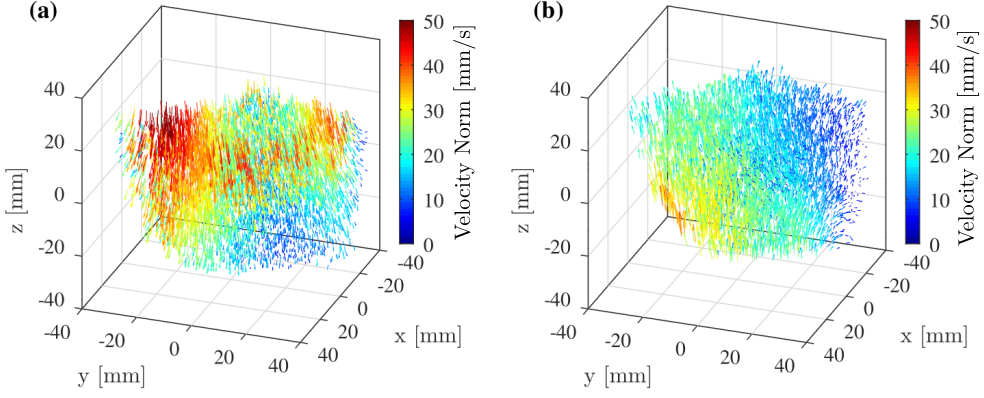


FIG. 17. Visualization of the recirculating mean flow for two 3D runs. (a) Run3D-2 with $f_{\text{mot}} = 6$ Hz and $S_{\text{mot}} = 20$ mm: downward flow of ~ 25 mm/s. (b) Run3D-7 under identical conditions: upward flow of ~ 17 mm/s.

setup is approximately $17 \times 17 \times 30$ mm³, a small fraction of the total 3D volume. The associated bias is thus expected to be limited.

To assess this quantitatively, we consider $\tilde{\mathbf{U}}$, the 3D mean flow truncated to the volume of a single 2×2D camera, and compute its depth-averaged version:

$$\tilde{\mathbf{U}}_{2D}(y, z) = \frac{1}{2L} \int_{-L}^L \tilde{\mathbf{U}}(x, y, z) dx,$$

with $L = 15$ mm. This projection is then duplicated along $x \in [-L, L]$ to span the full depth of field and allow pointwise comparison with $\tilde{\mathbf{U}}$ (see Fig. 18). Subtracting the two fields yields the residual, whose variance we compare to that of the turbulent velocity fluctuations.

We find that the impact of the projection is negligible (less than 3%) for the horizontal components, but can reach up to 20% for the vertical component. For this reason, the interpretation of the 2×2D measurements is restricted to the horizontal velocity components.

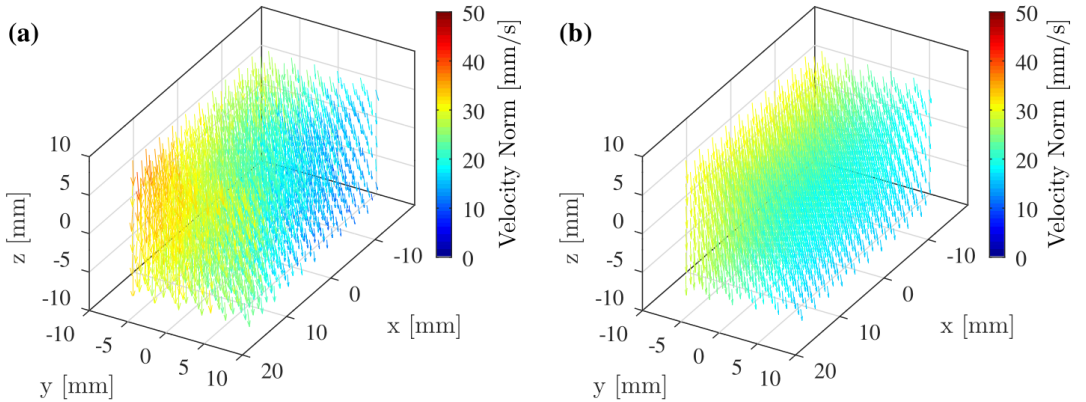


FIG. 18. Impact of the projection bias in 2×2D measurements, illustrated for Run3D-2. (a) Truncated 3D mean flow field, matching the volume of one 2×2D camera. (b) Field averaged along x and extended from $-L$ to $+L$ for comparison.

-
- [1] L. I. Dana and K. H. Onnes, Further experiments with liquid helium. b. a. preliminary determinations of the latent heat of vaporization of liquid helium, in *Proceedings of the Royal Academy of Amsterdam*, Vol. 29 (Proceedings of the Royal Academy of Amsterdam, 1926) pp. 1051–1061.
 - [2] M. Wolfke and W. H. Keesom, On the change of the dielectric constant of liquid helium with the temperature. provisional measurements., in *Proceedings of the Royal Academy of Amsterdam*, Vol. 31 (1927) pp. 81–89.
 - [3] W. H. Keesom and M. Wolfke, Two different liquid states af helium, in *Proceedings of the Royal Academy of Amsterdam*, Vol. 31 (1927) pp. 90–94.
 - [4] P. Kapitza, Viscosity of Liquid Helium below the λ -Point, *nat* **141**, 74 (1938).
 - [5] J. F. Allen and A. D. Misener, Flow of liquid helium ii, *Nature* **141**, 75 (1938).
 - [6] F. London, On the bose-einstein condensation, *Phys. Rev.* **54**, 947 (1938).
 - [7] L. Tisza, Transport phenomena in helium ii, *Nature* **141**, 913 (1938).
 - [8] L. Landau, Theory of the superfluidity of helium ii, *Phys. Rev.* **60**, 356 (1941).
 - [9] D. V. Osborne, The rotation of liquid helium ii, *Proceedings of the Physical Society. Section A* **63**, 909 (1950).
 - [10] L. Onsager, Statistical hydrodynamics, *Il Nuovo Cimento* (1943-1954) **6**, 279 (1949).
 - [11] R. Feynman, Chapter ii application of quantum mechanics to liquid helium (Elsevier, 1955) pp. 17–53.
 - [12] H. E. Hall, W. F. Vinen, and D. Shoenberg, The rotation of liquid helium ii i. experiments on the propagation of second sound in uniformly rotating helium ii, *Proceedings of the Royal Society of London. Series A. Mathematical and Physical Sciences* **238**, 204 (1956).
 - [13] H. E. Hall, W. F. Vinen, and D. Shoenberg, The rotation of liquid helium ii ii. the theory of mutual friction in uniformly rotating helium ii, *Proceedings of the Royal Society of London. Series A. Mathematical and Physical Sciences* **238**, 215 (1956).
 - [14] I. Bekarevich and I. M. Khalatnikov, Phenomenological derivation of the equations of vortex motion in he ii, *Sov. Phys. JETP* **13**, 643 (1961).
 - [15] P. L. Walstrom, I. Weisend, J. G., J. R. Maddocks, and S. W. van Sciver, Turbulent flow pressure drop in various He II transfer system components, *Cryogenics* **28**, 101 (1988).
 - [16] B. Rousset, G. Claudet, A. Gauthier, P. Seyfert, A. Martinez, P. Lebrun, M. Marquet, and R. Van Weelderren, Pressure drop and transient heat transport in forced flow single phase helium ii at high reynoldsnumbers, *Cryogenics* **34**, 317 (1994), fifteenth International Cryogenic Engineering Conference.
 - [17] S. Fuzier, B. Baudouy, and S. Van Sciver, Steady-state pressure drop and heat transfer in he ii forced flow at high reynolds number, *Cryogenics* **41**, 453 (2001).
 - [18] B. Rousset, P. Bonnay, P. Diribarne, A. Girard, J. M. Poncet, E. Herbert, J. Salort, C. Baudet, B. Castaing, L. Chevillard, F. Daviaud, B. Dubrulle, Y. Gagne, M. Gibert, B. Hébral, T. Lehner, P.-E. Roche, B. Saint-Michel, and M. Bon Mardion, Superfluid high REynolds von Kármán experiment, *Review of Scientific Instruments* **85**, 103908 (2014).
 - [19] B. Saint-Michel, E. Herbert, J. Salort, C. Baudet, M. Bon Mardion, P. Bonnay, M. Bourgoïn, B. Castaing, L. Chevillard, F. Daviaud, P. Diribarne, B. Dubrulle, Y. Gagne, M. Gibert, A. Girard, B. Hébral, T. Lehner, B. Rousset, and S. Collaboration, Probing quantum and classical turbulence analogy in von Kármán liquid helium, nitrogen, and water experiments, *Physics of Fluids* **26**, 125109 (2014).
 - [20] J. Maurer and P. Tabeling, Local investigation of superfluid turbulence, *Europhysics Letters (EPL)* **43**, 29 (1998).
 - [21] J. Salort, C. Baudet, B. Castaing, B. Chabaud, F. Daviaud, T. Didelot, P. Diribarne, B. Dubrulle, Y. Gagne, F. Gauthier, A. Girard, B. Hébral, B. Rousset, P. Thibault, and P.-E. Roche, Turbulent velocity spectra in superfluid flows, *Physics of Fluids* **22**, 125102 (2010).
 - [22] J. Salort, B. Chabaud, E. Lévêque, and P.-E. Roche, Energy cascade and the four-fifths law in superfluid turbulence, *Europhysics Letters* **97**, 34006 (2012).
 - [23] P.-E. Roche, C. F. Barenghi, and E. Leveque, Quantum turbulence at finite temperature: The two-fluids cascade, *Europhysics Letters* **87**, 54006 (2009).
 - [24] J. Salort, P.-E. Roche, and E. Leveque, Mesoscale equipartition of kinetic energy in quantum turbulence, *Europhysics Letters* **94**, 24001 (2011).
 - [25] W. F. Vinen and J. J. Niemela, Quantum turbulence, *Journal of Low Temperature Physics* **128**, 167 (2002).
 - [26] C. F. Barenghi, V. S. L'vov, and P.-E. Roche, Experimental, numerical, and analytical velocity spectra in turbulent quantum fluid, *Proceedings of the National Academy of Sciences* **111**, 4683 (2014).
 - [27] S. R. Stalp, L. Skrbek, and R. J. Donnelly, Decay of grid turbulence in a finite channel, *Phys. Rev. Lett.* **82**, 4831 (1999).

- [28] S. R. Stalp, J. J. Niemela, W. F. Vinen, and R. J. Donnelly, Dissipation of grid turbulence in helium ii, *Physics of Fluids* **14**, 1377 (2002).
- [29] J. Niemela, K. Sreenivasan, and R. Donnelly, Grid generated turbulence in helium ii, *Journal of Low Temperature Physics* **138**, 537 (2005).
- [30] S. Babuin, E. Varga, and L. Skrbek, The decay of forced turbulent coflow of he ii past a grid, *Journal of Low Temperature Physics* **175**, 324 (2014).
- [31] P. Walmsley, D. Zmeev, F. Pakpour, and A. Golov, Dynamics of quantum turbulence of different spectra, *Proceedings of the National Academy of Sciences* **111**, 4691 (2014).
- [32] S. Babuin, E. Varga, L. Skrbek, E. L  v  que, and P.-E. Roche, Effective viscosity in quantum turbulence: A steady-state approach, *Europhysics Letters* **106**, 24006 (2014).
- [33] W. Guo, M. L. Mantia, D. P. Lathrop, and S. W. V. Sciver, Visualization of two-fluid flows of superfluid helium-4, *Proceedings of the National Academy of Sciences* **111**, 4653 (2014).
- [34] P.   van  ara and M. La Mantia, Flows of liquid 4he due to oscillating grids, *Journal of Fluid Mechanics* **832**, 578–599 (2017).
- [35] C. Peretti, J. Vessaire, E. Durozoy, and M. Gibert, Direct visualization of the quantum vortex lattice structure, oscillations, and destabilization in rotating 4he, *Science Advances* **9**, eadh2899 (2023).
- [36] B. Rousset, C. Baudet, M. Bon-Mardion, M. Bourgoin, A. Braslau, F. Daviaud, P. Diribarne, B. Dubrulle, Y. Gagne, B. Gallet, M. Gibert, A. Girard, T. Lehner, I. Moukharski, and F. Sy, Cryogenic turbulence test facilities at CEA/SBT, IOP Conference Series: Materials Science and Engineering **101**, 012187 (2015).
- [37] N. F. I. Sy, *Turbulence de grille oscillante    basses temp  ratures*, Ph.D. thesis, Universit   Grenoble Alpes (2016).
- [38] F. Sy, P. Diribarne, B. Rousset, M. Gibert, and M. Bourgoin, Multiscale energy budget of inertially driven turbulence in normal and superfluid helium, *Phys. Rev. Fluids* **6**, 064604 (2021).
- [39] A. Srdic, H. J. S. Fernando, and L. Montenegro, Generation of nearly isotropic turbulence using two oscillating grids, *Experiments in Fluids* **20**, 395 (1996).
- [40] S. Shy, C. Tang, and S. Fann, A nearly isotropic turbulence generated by a pair of vibrating grids, *Experimental Thermal and Fluid Science* **14**, 251 (1997).
- [41] J. C. McLennan, H. D. Smith, and J. O. Wilhelm, Xiv. the scattering of light by liquid helium, *The London, Edinburgh, and Dublin Philosophical Magazine and Journal of Science* **14**, 161 (1932).
- [42] C. Bret, J. Chartier, P. Diribarne, J. Duplat, and B. Rousset, Controlled spherical deuterium droplets as Lagrangian tracers for cryogenic turbulence experiments, *Review of Scientific Instruments* **94**, 105114 (2023).
- [43] C. Bret, *Turbulence classique et quantique : Exp  riences et analyses comparatives*, Ph.D. thesis, Universit   Grenoble Alpe (2024).
- [44] F. Helml   and S. Scherer, Adaptive shape from focus with an error estimation in light microscopy, in *ISPA 2001. Proceedings of the 2nd International Symposium on Image and Signal Processing and Analysis. In conjunction with 23rd International Conference on Information Technology Interfaces (IEEE Cat.)* (IEEE, New York, 2001) pp. 188–193.
- [45] S. Babuin, M. Stammeier, E. Varga, M. Rotter, and L. Skrbek, Quantum turbulence of bellows-driven ⁴he superflow: Steady state, *Phys. Rev. B* **86**, 134515 (2012).
- [46] E. Varga, M. Jackson, D. Schmoranzner, and L. Skrbek, The use of second sound in investigations of quantum turbulence in he ii, *Journal of Low Temperature Physics* **197** (2019).
- [47] E. Woillez, J. Valentin, and P.-E. Roche, Second sound resonators and tweezers as vorticity or velocity probes: Fabrication, model, and method, *Review of Scientific Instruments* **94**, 105109 (2023).
- [48] W. Manthey, N. Kroemer, and V. Magori, Ultrasonic transducers and transducer arrays for applications in air, *Measurement Science and Technology* **3**, 249 (1992).
- [49] D. Anke, An air sound transducer for frequencies in the range 50 khz to 100 khz using the sell principle, *Acta Acustica united with Acustica* **30**, 30 (1974).
- [50] W. Zimmermann, Porous-membrane second-sound transducers for superfluid ⁴He, *Phys. Rev. B* **33**, 139 (1986).
- [51] J. Bertolaccini, E. L  v  que, and P.-E. Roche, Disproportionate entrance length in superfluid flows and the puzzle of counterflow instabilities, *Phys. Rev. Fluids* **2**, 123902 (2017).
- [52] R. J. Donnelly and C. F. Barenghi, The Observed Properties of Liquid Helium at the Saturated Vapor Pressure, *Journal of Physical and Chemical Reference Data* **27**, 1217 (1998).
- [53] As mentioned in Sec. III B, a shift of 8 μ bar is sufficient to shift the resonance frequency by approximately 1 Hz. The resulting phase shift depends on the damping coefficient α , but for the initial value $\alpha_0 = 1.5 \text{ m}^{-1}$, exciting the cavity 1 Hz off-resonance induces a phase shift of about 15   compared to the phase at exact resonance.
- [54] N. Mordant, A. Crawford, and E. Bodenschatz, Experimental lagrangian acceleration probability density

- function measurement, *Physica D: Nonlinear Phenomena* **193**, 245 (2004), anomalous distributions, nonlinear dynamics, and nonextensivity.
- [55] P. Švančara and M. La Mantia, Flight-crash events in superfluid turbulence, *Journal of Fluid Mechanics* **876**, R2 (2019).
 - [56] Y. Tang, S. Bao, T. Kanai, and W. Guo, Statistical properties of homogeneous and isotropic turbulence in ^4He measured via particle tracking velocimetry, *Phys. Rev. Fluids* **5**, 084602 (2020).
 - [57] N. Matsunaga, Y. Sugihara, T. Komatsu, and A. Masuda, Quantitative properties of oscillating-grid turbulence in a homogeneous fluid, *Fluid Dynamics Research* **25**, 147 (1999).
 - [58] E. J. Hopfinger and J.-A. Toly, Spatially decaying turbulence and its relation to mixing across density interfaces, *Journal of Fluid Mechanics* **78**, 155–175 (1976).
 - [59] I. P. D. De Silva and H. J. S. Fernando, Oscillating grids as a source of nearly isotropic turbulence, *Physics of Fluids* **6**, 2455 (1994).
 - [60] M. Ura, T. Komatsu, and N. Matsunaga, Entrainment due to oscillating-grid turbulence in two-layered fluid, in *Turbulence Measurements and Flow Modeling* (Hemisphere Publishing Corporation, Washington, 1987) pp. 109–118.
 - [61] M. Poulain-Zarcos, M. J. Mercier, and A. ter Halle, Global characterization of oscillating grid turbulence in homogeneous and two-layer fluids, and its implication for mixing at high peclet number, *Phys. Rev. Fluids* **7**, 054606 (2022).
 - [62] S. B. Pope, *Turbulent Flows* (Cambridge University Press, Cambridge, England, 2000).
 - [63] F. Moisy, P. Tabeling, and H. Willaime, Kolmogorov equation in a fully developed turbulence experiment, *Phys. Rev. Lett.* **82**, 3994 (1999).
 - [64] R. Ijsselstein, M. de Goeje, and H. Kramers, Combined measurements on various types of stationary flow of superfluid ^4He , *Physica B+C* **96**, 312 (1979).
 - [65] P. L. Walstrom, Heat transfer by internal convection in turbulent ^4He forced flow, *Journal of Low Temperature Physics* **73**, 391 (1988).
 - [66] D. S. Holmes and S. W. Van Sciver, Attenuation of second sound in bulk-flowing ^4He , *Journal of Low Temperature Physics*; (United States) **87:1-2**, 10.1007/BF00141568 (1992).
 - [67] T. V. Chagovets, A. V. Gordeev, and L. Skrbek, Effective kinematic viscosity of turbulent ^4He , *Phys. Rev. E* **76**, 027301 (2007).
 - [68] W. F. Vinen, How is turbulent energy dissipated in a superfluid?, *Journal of Physics: Condensed Matter* **17**, S3231 (2005).
 - [69] K. P. Iyer, K. R. Sreenivasan, and P. K. Yeung, Circulation in high reynolds number isotropic turbulence is a bifractal, *Phys. Rev. X* **9**, 041006 (2019).
 - [70] J. I. Polanco, P.-E. Roche, L. Danaila, and E. L  v  que, Disentangling temperature and reynolds number effects in quantum turbulence, *Proceedings of the National Academy of Sciences* **122**, e2426598122 (2025).
 - [71] S. P. McKenna and W. R. McGillis, Observations of flow repeatability and secondary circulation in an oscillating grid-stirred tank, *Physics of Fluids* **16**, 3499 (2004).